The Astrophysical Journal, 994:19 (22pp), 2025 November 20 https://doi.org/10.3847/1538-4357/ae071c

Asteroseismology of Carbon-deficient Red Giants: Merger Products of Hierarchical Triple Systems?

Sunayana Maben[1], Simon W. Campbell[2,3], Timothy R. Bedding[4], Gang Zhao[1,5], Madeline Howell[6], Yerra Bharat Kumar[7], and Bacham E. Reddy[8]
[1] CAS Key Laboratory of Optical Astronomy, National Astronomical Observatories, Chinese Academy of Sciences, Beijing 100101, People's Republic of China; sunayana.maben@gmail.com, gzhao@nao.cas.cn
[2] School of Physics and Astronomy, Monash University, Clayton, Victoria, Australia
[3] ARC Centre of Excellence for Astrophysics in Three Dimensions (ASTRO-3D), Australia
[4] Sydney Institute for Astronomy, School of Physics, University of Sydney, NSW 2006, Australia
[5] School of Astronomy and Space Science, University of Chinese Academy of Sciences, Beijing 100049, People's Republic of China
[6] Department of Astronomy, The Ohio State University, 140 W 18th Avenue, Columbus, OH 43210, USA
[7] Indian Institute of Astrophysics, 100ft road Koramangala, Bangalore, 560034, India
[8] Department of Physics, Indian Institute of Technology Jammu, Jammu 181221, India
Received 2025 June 24; revised 2025 September 8; accepted 2025 September 9; published 2025 November 11

Abstract

Carbon-deficient giants (CDGs) are a rare and chemically peculiar class of stars whose origins remain under active investigation. We present an asteroseismic analysis of the entire known CDG population, selecting 129 stars observed by Kepler, K2, and TESS to obtain seismic constraints. We detect solar-like oscillations in 43 CDGs. By measuring $\nu_{\rm max}$ and applying seismic scaling relations, we determine precise masses for these stars, finding that 79% are low mass ($M \lesssim 2\,M_{\odot}$). The luminosity distribution is bimodal, and the CDGs separate into three chemically and evolutionarily distinct groups, characterized by clear trends in sodium and CNO abundances, α-element enhancement, and kinematics. We find that two of these groups are only distinguished by their initial α-element abundances, thus effectively reducing the number of groups to two. Lithium enrichment is common across all groups, linking CDGs to lithium-rich giants and suggesting a shared evolutionary origin. We find that the spectroscopic $\log g$ is systematically offset from seismic values. Group 1 CDG patterns are most consistent with formation through core He-flash mixing, while the more massive and more chemically processed Groups 2 and 2α likely formed through mergers involving helium white dwarfs, possibly in hierarchical triples. Pollution from asymptotic giant branch stars appears very unlikely, given the unchanged [C+N+O] abundance across all groups.

Unified Astronomy Thesaurus concepts: Weak G band stars (1796); Chemically peculiar giant stars (1201); Asteroseismology (73); Low mass stars (2050); Stellar abundances (1577); Binary stars (154); Stellar mergers (2157)

Materials only available in the online version of record: machine-readable tables

1. Introduction

The study of carbon-deficient giants (CDGs) has a long history. More than a century ago, A. J. Cannon (1912) noticed that the red giant star HR 885 had an unusual spectrum, where the *G*-band—caused by CH molecular absorption—was not well defined, unlike in other G- and K-type stars. W. P. Bidelman (1951) closely examined the spectrum of this star and concluded that the *G*-band was absent. Later, W. P. Bidelman & D. J. MacConnell (1973) identified a group of G and K giants with extremely low carbon abundances, much lower than expected from the first dredge-up process. These stars, known as weak *G*-band (wGb) stars, exhibit very weak or absent CH molecular absorption at 4300 Å. More recently, H. E. Bond (2019) added five more CDGs to the previously known list of 39 wGb stars, bringing the total to 44. High-resolution spectroscopic studies (e.g., J. Adamczak & D. L. Lambert 2013; A. Palacios et al. 2016) confirmed that these stars not only have very low carbon abundances but also show low carbon isotopic ratios ($^{12}C/^{13}C \approx 3$–4) and enhanced nitrogen. Some of them are also enriched in lithium or sodium.

Earlier studies suggested that wGb stars are intermediate-mass stars ($M = 2.5$–$5.0\,M_{\odot}$) based on their positions in the Hertzsprung–Russell diagram. Most were found to be in the subgiant branch or red giant branch (RGB) phases, and a few were found in the red clump (RC) phase (e.g., A. Palacios et al. 2012; H. E. Bond 2019). However, new findings have revised this understanding. S. Maben et al. (2023b) and S. Maben et al. (2023a) expanded the known sample of CDGs by a factor of 3 by identifying around 100 additional stars using APOGEE survey data (Abdurro'uf et al. 2022). Their analysis of 15 CDGs in the Kepler field, incorporating asteroseismic mass determinations, revealed that these stars are predominantly low mass ($M \lesssim 2\,M_{\odot}$), in contrast to earlier findings. Remarkably, they also found that these CDGs are almost exclusively in the RC phase. Furthermore, a distinct pattern in their luminosity distribution led to the classification of CDGs into three groups. Possible formation scenarios for these stars include mergers between helium white dwarfs (HeWDs) and RGB stars, as well as binary mass transfer from asymptotic giant branch (AGB) stars. The overlap between

CDGs and lithium-rich giants suggests that they may share similar evolutionary origins (S. Maben et al. 2023a).

In this work, we extend the asteroseismic analysis of S. Maben et al. (2023a) to the full sample of 158 known CDGs (W. P. Bidelman 1951; W. P. Bidelman & D. J. MacConnell 1973; H. E. Bond 2019; N. Holanda et al. 2023; S. Maben et al. 2023a, 2023b), utilizing data from the Kepler, K2, and TESS missions. By combining asteroseismic information with astrometric, photometric, and spectroscopic data, we aim to refine mass estimates and to establish a more comprehensive evolutionary framework for CDGs. This approach is crucial because conventional spectroscopic analyses tend to underestimate $\log g$ in CDGs (A. Palacios et al. 2016), directly affecting mass determinations and highlighting the importance of asteroseismic constraints for both reliable mass estimates and accurate surface gravity measurements. Given the recent paradigm shift in our understanding of these stars, this study systematically classifies CDGs and investigates their formation mechanisms. By using multiple constraints on a larger sample, we provide new insights into their nature, formation, and evolution.

To address these aims, this paper is organized as follows. In Section 2, we describe the selection of the CDG sample through crossmatching with data from the Kepler, K2, and TESS missions. Section 3 details our methodology for estimating the frequency of the maximum oscillation power, $\nu_{\rm max}$, including light-curve preprocessing and power spectrum analysis using the `pyMON` pipeline. Section 4 presents the asteroseismic detections for the sample, examines their masses, chemical abundances, and kinematic properties, and identifies distinct subgroups with implications for their evolutionary origins. Our conclusions are summarized in Section 5.

2. Sample Selection

In the current study, we focus on the TESS, Kepler, and K2 fields because we are interested in obtaining asteroseismic constraints. We crossmatched the entire list of CDGs with stars observed by those three missions, resulting in a sample of 129 stars. Among these, 128 CDGs have TESS light curves, 17 have Kepler light curves, and 4 have K2 light curves.

We searched the literature for stars with previously published global asteroseismic parameters ($\nu_{\rm max}$ and $\Delta\nu$) and identified 27 stars. Among these, 16 are located in the Kepler field, with 15 included in the S. Maben et al. (2023a) study. All 16 Kepler stars have spectroscopic data from APOGEE and asteroseismic parameters derived from the Kepler light curves. Specifically, $\nu_{\rm max}$ and $\Delta\nu$ measurements are available for all 16 stars (B. Mosser et al. 2014; M. Vrard et al. 2016; J. Yu et al. 2018, 2020), while $\Delta\Pi_1$ values are reported for 11 of them (B. Mosser et al. 2014; M. Vrard et al. 2016). Among the remaining 11 stars with published asteroseismic parameters, all have $\nu_{\rm max}$ derived from TESS light curves (M. Hon et al. 2021; J. Zhou et al. 2024), and 3 also have $\Delta\nu$ reported in J. Zhou et al. (2024).

In summary, we have 27 CDGs with global asteroseismic parameters determined in the literature, and 102 CDGs that do not. We aim to determine asteroseismic parameters for as many of these 129 CDGs as possible.

3. Methodology

Asteroseismology typically uses both the large frequency separation ($\Delta\nu$) and the frequency of the maximum oscillation power ($\nu_{\rm max}$) to determine stellar properties such as mass and radius (e.g., W. J. Chaplin & A. Miglio 2013). However, in this study, we focus solely on measuring $\nu_{\rm max}$ because the determination of $\Delta\nu$ is highly uncertain due to the limited amount of observational data available for most stars in our sample. This limitation is especially significant for the 111 CDGs with TESS data alone, where 79 stars (71%) have been observed in fewer than five TESS sectors, limiting the signal-to-noise ratio (SNR) and frequency resolution of the power spectra.

Similar challenges have been noted in previous studies, where data limitations restrict a reliable $\Delta\nu$ estimation (e.g., M. Hon et al. 2021; D. Stello et al. 2022; M. Howell et al. 2025). Given that $\nu_{\rm max}$, when combined with temperature and luminosity, has been shown to be sufficient for deriving accurate asteroseismic masses (e.g., M. Hon et al. 2021; M. Howell et al. 2022; S. P. Malla et al. 2024), we adopt this approach in our analysis.

The steps to measure $\nu_{\rm max}$ can be summarized as follows:

1. Calculate an initial estimate of $\nu_{\rm max}$ based on the standard scaling relation (Section 3.1).
2. Calculate the power density spectrum of the light curve (Section 3.2).
3. Measure $\nu_{\rm max}$ and its associated uncertainty (Section 3.3).

3.1. Initial Estimate of ν_{max}

An initial estimate of $\nu_{\rm max}$ is required for each star, as steps (ii)–(iii) depend on this parameter. To obtain this estimate, we employed the standard scaling relation (T. M. Brown et al. 1991; H. Kjeldsen & T. R. Bedding 1995):

$$\nu_{\rm max} \simeq \nu_{\rm max,\odot}\left(\frac{g}{g_\odot}\right)\left(\frac{T_{\rm eff}}{T_{\rm eff,\odot}}\right)^{-1/2}, \quad (1)$$

where we adopted $\nu_{\rm max,\odot} = 3090 \pm 30\ \mu$Hz (D. Huber et al. 2011), $T_{\rm eff,\odot} = 5772$ K (A. Prša et al. 2016), and $\log g_\odot = 4.44$ (T. Morel et al. 2014) as our solar reference values.

The effective temperatures ($T_{\rm eff}$) and surface gravities (g) for the CDGs were taken from the literature (J. Adamczak & D. L. Lambert 2013; A. Palacios et al. 2016; N. Holanda et al. 2023; S. Maben et al. 2023a, 2023b; N. Holanda et al. 2024). In cases where these parameters were not available, we used values from Gaia DR3 (Gaia Collaboration et al. 2016, 2023). The available values of $\log g$ are not particularly accurate—indeed, refining these values using asteroseismology is one our main aims—but they suffice for giving an initial estimate of $\nu_{\rm max}$.

3.2. Preprocessing Light Curves and Calculating Power Spectra

We downloaded all available light curves for the CDGs from the Mikulski Archive for Space Telescopes[9] (MAST) using the Python package `lightkurve` (Lightkurve Collaboration et al. 2018). These light curves have been extracted and detrended using mission-specific pipelines: Kepler (J. M. Jenkins et al. 2010), K2 (A. Vanderburg & J. A. Johnson 2014; R. Luger et al. 2016), and TESS (J. M. Jenkins et al. 2016; D. A. Caldwell et al. 2020;

[9] https://mast.stsci.edu/portal/Mashup/Clients/Mast/Portal.html

C. X. Huang et al. 2020a, 2020b). We included all TESS data available up to the end of Sector 81 (2024 August 10). We performed a quality assessment of each light curve through visual inspection, evaluating them for systematic trends, instrumental artifacts, and noise levels. We then selected those light curves with minimal contamination for further analysis, ensuring that only high-quality data from Kepler quarters, K2 campaigns, and TESS sectors were used. This resulted in a modest fraction of the data being discarded (161 sectors for 40 different stars).

To eliminate low-frequency variations caused by stellar activity and instrumental noise—often not corrected for by PDCSAP from the Kepler and TESS missions (J. C. Smith et al. 2012; J. M. Jenkins et al. 2016)—we applied a high-pass filter to each light curve, as follows. We divided Kepler light curves into two segments per quarter, and we divided TESS light curves into four half-orbits per sector (giving segments of approximately 7 days each), to account for flux jumps caused by momentum dumping. The high-pass filter was applied to each segment by dividing the original flux by a smoothed version of the light curve, obtained through convolution with a Gaussian kernel. The filter cutoff, set by the width of the Gaussian, was varied from star to star, based on the estimated $\nu_{\rm max}$ from the previous step. The cutoff frequency was set well below this value to ensure that the filter did not interfere with the oscillations under study. This adaptive filtering technique allowed us to effectively reduce low-frequency noise while preserving higher-frequency oscillations.

Next, we concatenated the light curves from all available sectors and calculated power spectra up to the Nyquist frequency. The power (in ppm^2) was converted to power density (in ppm^2 μHz^{-1}) by multiplying by the effective time span of the observations (H. Kjeldsen & T. R. Bedding 1995).

We identified three stars, HD 124721, HD 40402, and BD+5 593, that exhibited anomalous peaks in their power spectra, likely indicative of contamination by a close binary (I. L. Colman et al. 2017). Notably, HD 124721 and HD 40402 have been found to be in either multiple systems or binary systems in different catalogs (B. D. Mason et al. 2001; J. Dommanget & O. Nys 2002; K. El-Badry et al. 2021). For example, the power spectrum of HD 124721, calculated from a single sector of TESS data, which features an anomalous high-amplitude peak and its second harmonic, is shown in Appendix A. These strong peaks were removed to refine our analysis. Such signals are typically attributed to either chance alignments with unrelated binary systems or physical associations in hierarchical triples (I. L. Colman et al. 2017). This observation highlights the complexity of stellar interactions and the necessity for careful interpretation of power spectra in the context of binary and multiple star systems.

3.3. Measuring ν_{max}

To measure $\nu_{\rm max}$—and its associated uncertainty—we used the `pyMON` pipeline[10] (M. Howell et al. 2025), which is directly based on `pySYD` (D. Huber et al. 2009; A. Chontos et al. 2022). The `pyMON` pipeline is ideal for our purpose because it is optimized for measuring $\nu_{\rm max}$ in low SNR data, and for low-$\nu_{\rm max}$ giants (M. Howell et al. 2025).

The initial estimate of $\nu_{\rm max}$ is used by `pyMON` to define the power excess window where oscillations are expected, which can be further refined with optional lower and upper frequency limits if the data are noisy. The background is removed from the power spectrum by subtracting a linear model derived from the intersection between the power excess window boundaries (see Figure 1 and Appendix D for examples). This tends to work more consistently for stars with low $\nu_{\rm max}$, where there are too few low-frequency data points to reliably constrain a Harvey-like granulation model (M. Howell et al. 2025). Following this, the spectrum is heavily smoothed, guided by a $\Delta\nu$ estimate based on the $\Delta\nu$–$\nu_{\rm max}$ scaling relation, as described by D. Stello et al. (2009). The frequency corresponding to the maximum power within the power excess window is adopted as $\nu_{\rm max}$. The pipeline performs this analysis in a single pass, relying on the initial $\nu_{\rm max}$ estimate, consistent with its `pySYD`-based approach. To determine the uncertainty, stochastic noise is introduced into the power spectrum, and $\nu_{\rm max}$ is reestimated. This process is repeated 500 times, and the standard deviation of the resulting $\nu_{\rm max}$ distribution serves as the uncertainty estimate, consistent with the approach of D. Huber et al. (2009).

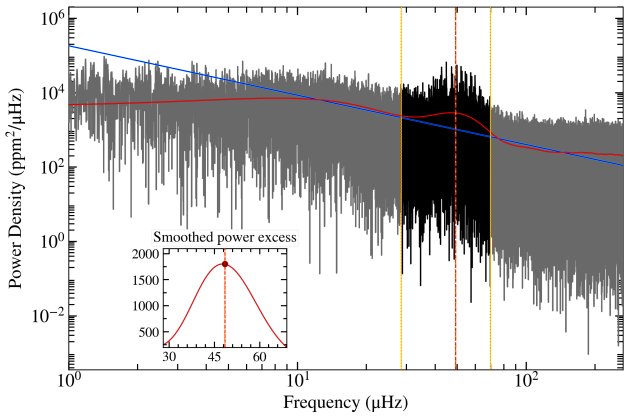

Figure 1. Power spectrum of 2M19125144+3850261 (gray), including the smoothed power spectrum (red) and the linear background fit (blue). The power excess (black) is positioned between two vertical yellow lines, which mark the window. The vertical red dashed line represents the measured $\nu_{\rm max}$ at 49 μHz. The `pyMON` pipeline estimates $\nu_{\rm max}$ as the frequency of maximum power in the background-corrected smoothed power spectrum (shown in inset).

Our analysis of 129 CDGs using TESS, Kepler, and K2 data resulted in clear detections of solar-type oscillations in 43 CDGs, which constitutes 33% of the sample. The detailed detection statistics are presented in Section 4.2.

With $\nu_{\rm max}$ determined, we applied the following asteroseismic scaling relation to derive the stellar mass (D. Stello et al. 2008):

$$\left(\frac{M}{M_\odot}\right) \simeq \left(\frac{\nu_{\rm max}}{\nu_{\rm max,\odot}}\right)\left(\frac{L}{L_\odot}\right)\left(\frac{T_{\rm eff}}{T_{\rm eff,\odot}}\right)^{-7/2}. \quad (2)$$

Note that this uses the luminosity determined as described in Section 4.4.1 and the spectroscopic effective temperature, but not the spectroscopic estimate of surface gravity.

4. Results and Discussion

4.1. Comparison with Published $\nu_{\rm max}$ Values

As a check, we present a comparative analysis for 27 CDGs between the published $\nu_{\rm max}$ values and our values obtained using the `pyMON` pipeline (see Table B1 and Figure 2). Our goal is to assess how our measured values align with those reported in the literature.

[10] https://github.com/maddyhowell/pyMON

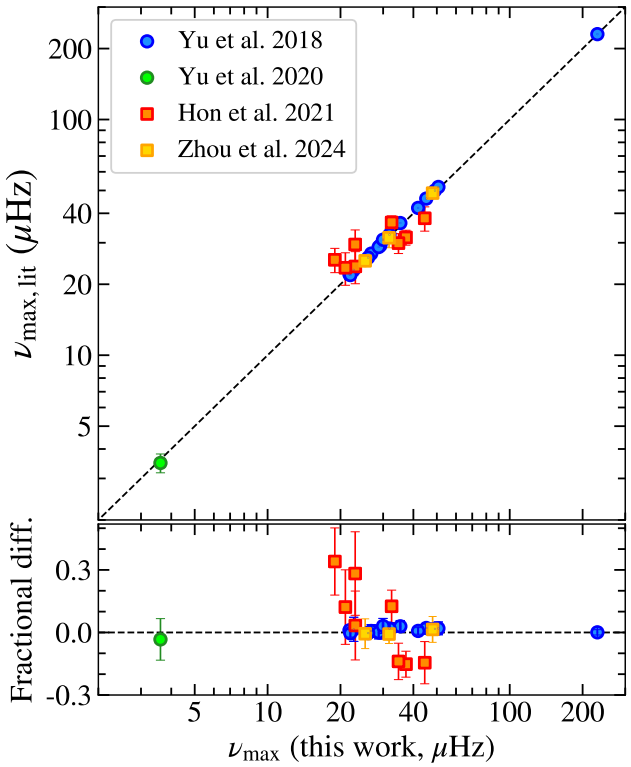

Figure 2. Comparison of the $\nu_{\rm max}$ values obtained using pyMON (this work) with literature values ($\nu_{\rm max,\,lit}$) from Kepler (J. Yu et al. 2018, 2020) and TESS (M. Hon et al. 2021; J. Zhou et al. 2024; see Table B1). The diagonal black line indicates the one-to-one relation. The bottom panel shows the fractional difference, defined as $(\nu_{\rm max,\,lit} - \nu_{\rm max})/\nu_{\rm max}$. Apart from the M. Hon et al. (2021) sample, the agreement between our values and those in the literature is excellent (see text for details).

When compared with J. Yu et al. (2018, 2020), who used 4 yr Kepler data, and J. Zhou et al. (2024), who used 2 minute cadence TESS data from sectors 1 to 60, the mean fractional difference is 0.7% with a standard deviation of 1.5%. This close agreement demonstrates that our $\nu_{\rm max}$ measurements are consistent with those derived from the same or similar data sets.

In contrast, the comparison with M. Hon et al. (2021), who employed 30 minute cadence TESS light curves from sectors 1 to 26, shows larger discrepancies (see the examples in Appendix D). These arise primarily from the more limited data coverage available in that study, which affects the precision of the $\nu_{\rm max}$ measurements and leads to increased scatter. Given these differences in data quality and coverage, we exclude the M. Hon et al. (2021) sample from our main quantitative comparison, but note that our results remain broadly consistent within the uncertainties.

For stars observed with Kepler, and with TESS at 2 minute cadence, the typical relative uncertainties in the $\nu_{\rm max}$ measurements range from 1% to 5%. For most stars, the differences between our values and those from the literature fall within 1σ–2σ of the combined uncertainties, indicating that the observed scatter is consistent with expected measurement errors.

These $\nu_{\rm max}$ differences propagate directly into the seismic mass estimates, as evidenced by our comparative analysis of masses derived using both pyMON and literature $\nu_{\rm max}$ values (see Section 4.4.2). According to the standard asteroseismic scaling relation (Equation (2)), the seismic mass scales linearly with $\nu_{\rm max}$, meaning that a proportional offset in $\nu_{\rm max}$ would translate to the same percentage difference in the derived masses, assuming other parameters remain constant.

In summary, our measured $\nu_{\rm max}$ values, derived using the pyMON pipeline, show good overall agreement with those reported in the literature, and excellent agreement with studies that utilized similar amounts of data.

Table 1
Summary of Solar-type Oscillation Detections among the CDGs

Detection Status	Number of CDGs	Percentage %
Clear detection	43	33.3
Marginal detection	9	7.0
No detection	77	59.7

4.2. Discussion of $\nu_{\rm max}$ Measurements

Table 1 summarizes the detection statistics for solar-type oscillations among the CDGs. We found that 43 CDGs exhibit clear detections of solar-type oscillations, constituting 33.3% of the sample, with 16 derived from Kepler light curves and 27 from TESS light curves (see Table 2). In contrast, 9 CDGs (7.0%) show marginal detections (see Table C1), while 77 CDGs (59.7%) exhibit no detectable oscillations with the available data. We note that this latter group includes many stars with limited data or sector coverage, so the true fraction of oscillating CDGs may be higher, and the 59.7% should be considered an upper limit on the nondetection rate. The majority of the nondetections came from TESS light curves (see Table C2 and Section 4.2).

A key science question in this study is to deduce the origins of CDGs, which requires careful consideration of observational biases that may affect our sample. To investigate this, Figure 3 presents histograms of various stellar parameters for CDGs, categorized by their $\nu_{\rm max}$ detection levels: clear detection, marginal detection, and no detection. These distributions allow us to examine how different observational and intrinsic properties influence oscillation detectability and to determine whether biases exist that could affect our conclusions about CDG origins.

Figure 3(a) shows apparent magnitudes, estimated from color–color transformations in M. Riello et al. (2021) relating Gaia DR3 to Johnson–Cousins photometry (P. B. Stetson 2000). CDGs with clear $\nu_{\rm max}$ detections are brighter/nearby stars, typically $m_V \leqslant 12$. Panel (b) shows absolute magnitudes. CDGs with clear detections cluster around $M_V \approx -0.2$, whereas stars with no detections exhibit a broader range of absolute magnitudes. This suggests the nondetected sample is not biased toward specific magnitudes. The similarity of the distribution to the overall sample implies no strong evolutionary bias in $\nu_{\rm max}$ detection. Panel (d) shows luminosities, determined as in Section 4.4.1. CDGs with clear detections have $\log(L/L_\odot) \approx 2.1 \pm 0.3$ dex. Nondetections occur at high luminosity because these stars exhibit lower oscillation frequencies (low $\nu_{\rm max}$), which are hard to resolve with a light curve of limited duration (insufficient frequency resolution). Indeed, the majority of nondetections are based on TESS data (there was only one from Kepler and two from K2). This reflects the fact that the observational limitation is the SNR, which significantly influences detectability (e.g., D. Stello et al. 2022). In particular, fainter and intrinsically less

Table 2
Atmospheric Parameters Along with Our Asteroseismic Measurements and Mass Estimates from Equations (2) and (4) of the CDGs

Star	KIC/TIC	$T_{\rm eff}$ (K)	$\log g$	$\log(L/L_{\odot})$	$\nu_{\rm max}$ (μHz)	$M_{\rm seismic}$ ($M_{\odot}$)	$M_{\rm spec}$ ($M_{\odot}$)
2M19581582+4055411	5737930	4443 ± 50	1.78 ± 0.05	2.77 ± 0.07	3.61 ± 0.17	1.72 ± 0.30	3.67 ± 0.75
2M19055092+3745351	2423824	5007 ± 50	2.27 ± 0.05	2.15 ± 0.05	21.79 ± 0.12	1.64 ± 0.20	1.69 ± 0.28
2M19252454+4036484	5446927	5107 ± 50	2.30 ± 0.05	2.05 ± 0.05	21.97 ± 0.10	1.22 ± 0.15	1.33 ± 0.22
2M19090355+4407005	8222189	4914 ± 50	2.37 ± 0.05	2.17 ± 0.04	22.68 ± 0.36	1.91 ± 0.19	2.40 ± 0.37
2M19211488+3959431	4830861	4959 ± 50	2.46 ± 0.05	2.14 ± 0.05	26.02 ± 0.14	1.98 ± 0.20	2.65 ± 0.41
2M19382715+3827580	3355015	4846 ± 50	2.35 ± 0.05	1.81 ± 0.05	26.79 ± 0.13	1.03 ± 0.13	1.06 ± 0.18
2M19442885+4354544	8110538	4975 ± 50	2.25 ± 0.05	1.98 ± 0.05	28.76 ± 0.15	1.49 ± 0.18	1.12 ± 0.19
2M19400612+3907470	4071012	4992 ± 50	2.56 ± 0.05	2.07 ± 0.04	29.21 ± 0.14	1.85 ± 0.18	2.77 ± 0.42
2M19340082+4108491	5881715	4840 ± 50	2.37 ± 0.05	1.89 ± 0.05	29.97 ± 0.24	1.39 ± 0.17	1.34 ± 0.22
2M19422093+5018436	11971123	4848 ± 50	2.48 ± 0.05	1.79 ± 0.04	31.87 ± 0.24	1.17 ± 0.12	1.29 ± 0.20
2M19404764+3942376	4667911	4740 ± 50	2.42 ± 0.05	1.67 ± 0.04	35.33 ± 0.24	1.07 ± 0.11	0.98 ± 0.15
2M19133911+4011046	5000307	5018 ± 50	2.62 ± 0.05	1.75 ± 0.04	41.85 ± 0.18	1.24 ± 0.12	1.46 ± 0.22
2M19181645+4506527	8879518	4832 ± 50	2.72 ± 0.05	1.73 ± 0.04	45.21 ± 0.22	1.46 ± 0.15	2.08 ± 0.32
2M19125144+3850261	3736289	4978 ± 50	2.58 ± 0.05	1.80 ± 0.04	49.09 ± 0.24	1.68 ± 0.17	1.59 ± 0.24
2M19565550+4330561	7848354	5004 ± 50	2.66 ± 0.05	1.75 ± 0.06	50.74 ± 0.29	1.52 ± 0.22	1.65 ± 0.30
2M19052312+4422242	8352953	5101 ± 50	3.34 ± 0.05	1.10 ± 0.04	230.13 ± 0.40	1.45 ± 0.14	1.64 ± 0.25
2M16405512+6435204	198279370	4591 ± 50	2.02 ± 0.05	2.83 ± 0.04	5.67 ± 0.18	2.76 ± 0.29	6.44 ± 0.72
2M07263003+4230102	67885101	4766 ± 50	2.14 ± 0.05	2.30 ± 0.05	11.11 ± 0.34	1.40 ± 0.18	2.15 ± 0.28
2M05272526+0317520	457250848	5057 ± 50	2.04 ± 0.05	2.45 ± 0.07	11.23 ± 0.34	1.63 ± 0.27	1.90 ± 0.34
HD 91622[a]	392847860	4457 ± 50	1.63 ± 0.10	2.27 ± 0.05	11.42 ± 0.20	1.70 ± 0.21	0.81 ± 0.21
2M05485828-0335586	176582672	4614 ± 50	1.95 ± 0.05	2.10 ± 0.06	12.62 ± 0.51	1.13 ± 0.17	1.00 ± 0.15
HD 102851	94550436	4991 ± 41	2.68 ± 0.26	2.42 ± 0.04	13.31 ± 0.34	1.88 ± 0.19	8.18 ± 4.96
2M04024317+1638559	243013051	4826 ± 50	2.26 ± 0.05	2.35 ± 0.05	13.66 ± 0.09	1.85 ± 0.22	3.03 ± 0.40
2M05301788+0140466	138827843	5130 ± 50	2.44 ± 0.05	1.93 ± 0.06	14.70 ± 0.34	0.61 ± 0.09	1.36 ± 0.22
HD 91805	146431583	5247 ± 15	2.56 ± 0.04	2.46 ± 0.04	15.19 ± 0.47	1.98 ± 0.19	5.59 ± 0.73
HD 49960	52980877	5030 ± 32	2.61 ± 0.05	2.28 ± 0.06	16.32 ± 0.51	1.63 ± 0.23	4.89 ± 0.89
2M05120630-5913438	358459098	4998 ± 50	2.35 ± 0.05	1.80 ± 0.04	18.95 ± 0.42	0.64 ± 0.07	0.92 ± 0.10
HD 31869	738036	4800 ± 100	1.80 ± 0.18	2.30 ± 0.05	19.33 ± 0.51	2.38 ± 0.33	0.96 ± 0.42
2M00230981+7152126	363760185	4823 ± 50	2.26 ± 0.05	2.07 ± 0.05	20.60 ± 0.34	1.47 ± 0.18	1.59 ± 0.21
BD+5 593	283623989	5045 ± 60	2.50 ± 0.18	2.08 ± 0.05	20.95 ± 0.51	1.31 ± 0.16	2.37 ± 1.03
HD 78146	37923103	4734 ± 96	2.13 ± 0.03	2.27 ± 0.05	22.11 ± 0.51	2.67 ± 0.37	2.02 ± 0.32
2M06022767-6209038	149989441	4946 ± 50	2.40 ± 0.05	2.11 ± 0.04	23.00 ± 0.77	1.65 ± 0.17	2.19 ± 0.55
HD 56438	134545196	5037 ± 163	2.75 ± 0.01	2.19 ± 0.05	23.03 ± 0.86	1.86 ± 0.31	5.47 ± 0.96
HD 18474	192247771	5198 ± 38	2.65 ± 0.03	2.15 ± 0.04	25.29 ± 0.48	1.67 ± 0.16	3.50 ± 0.42
HD 82595	5480307	4995 ± 79	2.28 ± 0.01	2.35 ± 0.04	25.58 ± 0.51	3.07 ± 0.34	2.76 ± 0.32
HD 94956	363418244	5131 ± 75	2.76 ± 0.30	2.16 ± 0.05	26.27 ± 0.86	1.86 ± 0.24	4.85 ± 3.41
HD 201557	231638013	4730 ± 90	2.15 ± 0.18	2.19 ± 0.05	31.74 ± 0.30	3.19 ± 0.43	1.77 ± 0.77
HD 18636	321087542	5085 ± 80	2.70 ± 0.18	1.68 ± 0.04	32.52 ± 0.69	0.78 ± 0.09	1.45 ± 0.62
HD 54627	134282943	4990 ± 70	2.55 ± 0.16	2.06 ± 0.05	33.33 ± 1.20	2.06 ± 0.27	2.65 ± 1.03
HD 124721	242443733	5107 ± 61	2.64 ± 0.11	2.13 ± 0.04	34.72 ± 1.03	2.33 ± 0.25	3.50 ± 0.96
HD 16424	441127020	4850 ± 40	2.60 ± 0.10	1.95 ± 0.04	37.27 ± 0.34	1.98 ± 0.19	2.58 ± 0.65
HD 40402	153122373	5005 ± 110	2.80 ± 0.18	2.16 ± 0.05	44.56 ± 0.34	3.43 ± 0.48	5.86 ± 2.57
HD 166208	332626441	5177 ± 52	2.81 ± 0.04	2.04 ± 0.04	48.03 ± 1.26	2.49 ± 0.59	3.99 ± 1.00

Notes. All stellar designations beginning with "2M" denote the APOGEE ID of the carbon-deficient giants identified using APOGEE data. For these stars, we adopt the errors in $T_{\rm eff}$ and [Fe/H] as 50 K and 0.05 dex, respectively. The first 16 rows contain Kepler Input Catalog (KIC) IDs, while the remaining rows contain TESS Input Catalog (TIC) IDs. A horizontal line is used to visually separate stars observed with Kepler from those observed with TESS.
[a] $T_{\rm eff}$ and $\log g$ are from T. Matsuno et al. (2024).

(This table is available in machine-readable form in the online article.)

luminous stars often have an SNR inadequate for detecting their oscillations (D. Stello et al. 2022). Panel (c) shows lower reddening for clear detections, from the 3D dust map of G. M. Green et al. (2019) or, where unavailable, from D. J. Schlegel et al. (1998) recalibrated by E. F. Schlafly & D. P. Finkbeiner (2011). This is likely due to proximity.

Figures 3(e) and (f) show the distributions of effective temperature and surface gravity, respectively, with values taken from the literature (J. Adamczak & D. L. Lambert 2013; A. Palacios et al. 2016; N. Holanda et al. 2023, 2024; S. Maben et al. 2023a, 2023b). Clear detections occur at $T_{\rm eff} \approx 4900 \pm 200$ K and $\log g \approx 2.4 \pm 0.3$ dex. This is consistent with RC stars expected at $\log g \approx 2.4$ (J. Yu et al. 2018). No clear detections appear at the cooler $T_{\rm eff} \approx 4000$–4500 K or lower $\log g \approx 0.5 - 1.5$. This confirms that cooler, larger giants with low $\nu_{\rm max}$ are underrepresented in the asteroseismic detections. This again reflects that fact that the detection of solar-like oscillations becomes increasingly difficult for stars with low $\nu_{\rm max}$, due to insufficient frequency resolution. Panels (g) and (h) of Figure 3 present the distributions of [C/Fe] and [Na/Fe], respectively. Clear detections favor extreme [C/Fe] compositions. They also

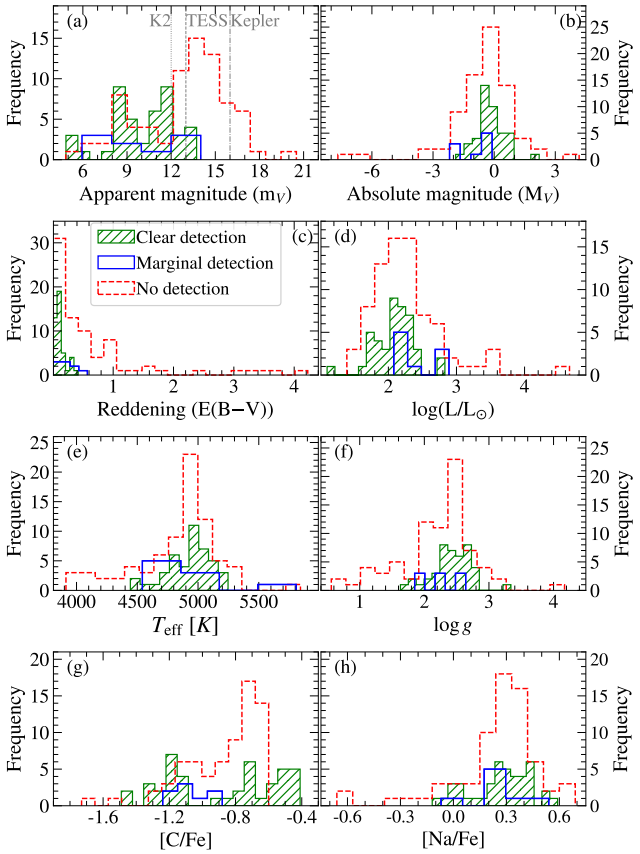

Figure 3. Histograms of various stellar parameters for CDGs, color-coded by $\nu_{\rm max}$ detection level: green (clear), blue (marginal), and red (no detection). Panels (a) and (b) show the distributions of apparent and absolute magnitudes, respectively. In panel (a), vertical lines indicate the apparent magnitude detection limits for the K2, TESS, and Kepler missions, respectively. Panels (c) and (d) display the distributions of reddening and luminosity. Panels (e) and (f) present the distributions of effective temperature and spectroscopic surface gravity. Finally, panels (g) and (h) illustrate the distributions of [C/Fe] and [Na/Fe] abundance ratios. We use the solar abundance of C and Na as derived by N. Grevesse et al. (2007). The CDG HD 91622, which exhibits clear detections of solar-type oscillations, lacks literature values for $T_{\rm eff}$ and log g; therefore, these parameters were taken from photometric measurements in T. Matsuno et al. (2024). Notably, HD 91622 is not included in the distributions of [C/Fe] and [Na/Fe]. See text for details.

show a secondary bias toward moderate [C/Fe] compositions. The sodium abundance distribution remains similar between CDGs with and without clear detections.

In summary, our analysis of $\nu_{\rm max}$ detection rates in CDGs reveals that successful detections are primarily limited by observational constraints, with clear biases toward brighter, warmer stars with properties consistent with RC stars. The underrepresentation of cooler, more luminous giants with low $\nu_{\rm max}$ values in our sample highlights the technical challenges in resolving low-frequency oscillations, particularly with TESS data, while the preference for carbon-poor compositions suggests a potential connection between stellar chemistry and oscillation properties.

4.3. Comparison of Expected and Observed $\nu_{\rm max}$

In Figure 4, we compare the expected $\nu_{\rm max}$, derived from spectroscopic values for log g and $T_{\rm eff}$ using Equation (1), with the observed $\nu_{\rm max}$ for our sample of CDGs, together with a large sample of RGB and RC stars from J. Yu et al. (2018).

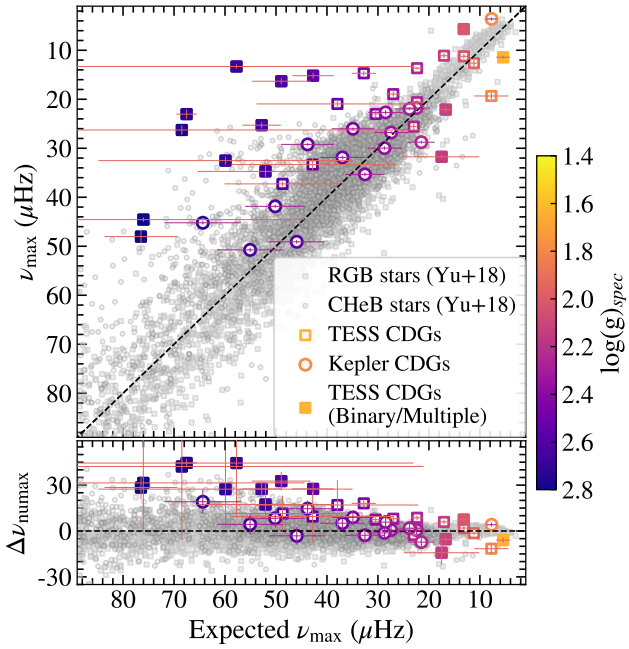

Figure 4. Comparison of the expected $\nu_{\rm max}$ values (using Equation (1)) against the observed $\nu_{\rm max}$ for the CDGs exhibiting clear detections of solar-type oscillations. Giants classified based on asteroseismic analysis form the background from J. Yu et al. (2018; see key). Their expected $\nu_{\rm max}$ values were calculated using $T_{\rm eff}$ and log g values taken from APOGEE DR17 (Abdurro'uf et al. 2022). The color bar indicates the spectroscopic surface gravity of each CDG. Large open circles represent our Kepler CDGs, while open squares indicate our TESS CDGs. The CDGs that are reported to be in multiple systems or in a binary system in the literature are filled with colors corresponding to their spectroscopic surface gravity. KIC 8352953, which is classified as an RGB star in J. Yu et al. (2018) and has a $\nu_{\rm max} \approx 230$ μHz, corresponding to the lower-RGB phase, is not included. The bottom panel shows the star-by-star residuals between expected $\nu_{\rm max}$ and observed $\nu_{\rm max}$, expressed in units of μHz. See text for details.

To identify binaries and multiple systems in our sample, we crossmatched the CDGs with several established catalogs: the Washington Visual Double Star catalog (B. D. Mason et al. 2001), the Catalog of Components of Double and Multiple Stars (J. Dommanget & O. Nys 2002), an extensive catalog of Gaia eDR3 binary stars within ≈1 kpc of the Sun[11] (K. El-Badry et al. 2021), the catalog of stellar and substellar companions identified using Gaia DR2 and EDR3 proper-motion anomalies (P. Kervella et al. 2019, 2022), and the Binary Star Database (D. Kovaleva et al. 2015). This analysis identified 14 out of 43 CDGs as binaries or multiple systems, which are marked with filled symbols in Figure 4.

Most single CDGs lie close to the one-to-one line, indicating good agreement between expected and observed $\nu_{\rm max}$. In contrast, binaries and multiple systems display the largest discrepancies, with observed $\nu_{\rm max}$ values systematically lower than expected. This trend is especially clear in the residuals shown in the bottom panel of Figure 4. The larger horizontal error bars for binaries reflect greater uncertainties in the spectroscopic log g and $T_{\rm eff}$, which further complicate the prediction of $\nu_{\rm max}$ for these systems.

For single stars, we find that the median residual, defined as the difference between the expected and observed $\nu_{\rm max}$, is 5.1 μHz when using APOGEE spectroscopic parameters and 27.4 μHz when using optical spectroscopy, indicating larger

[11] We note that Gaia catalog is of spatially resolved binaries only.

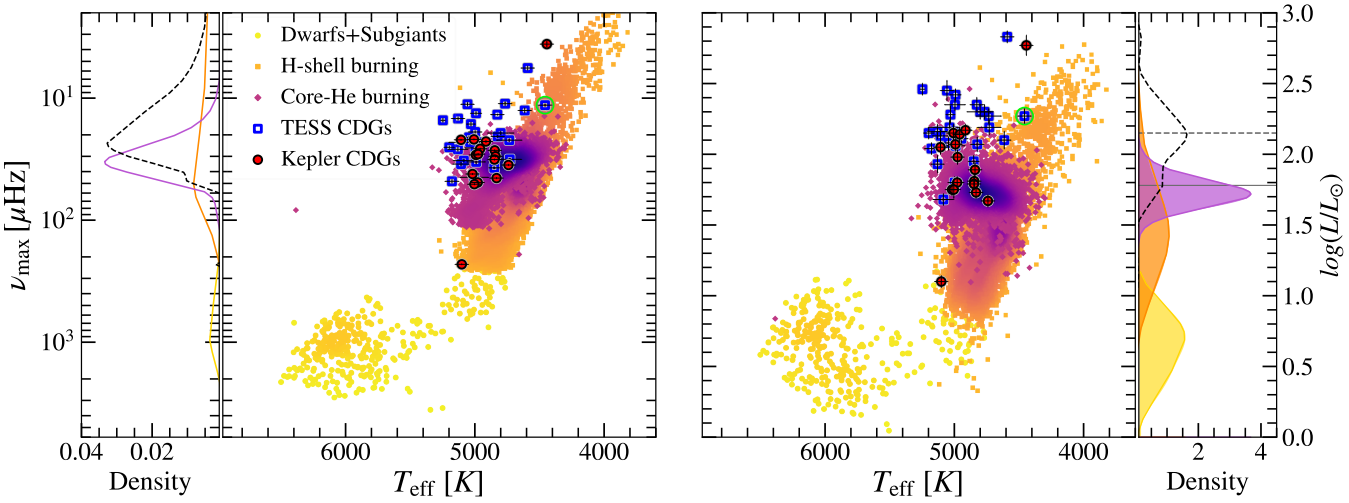

Figure 5. Left panel: asteroseismic Hertzsprung–Russell diagram (ν_{max} vs. T_{eff}). Right panel: Hertzsprung–Russell diagram. The ν_{max} estimates were adopted from A. Serenelli et al. (2017) for the dwarfs and subgiants (yellow symbols), M. H. Pinsonneault et al. (2018) and J. Yu et al. (2018) for the first-ascent RGB stars (orange symbols), and He-core burning giants (purple symbols). Their estimates of T_{eff} were taken from APOGEE DR17 (Abdurro'uf et al. 2022), and luminosity estimates were taken from the Gaia DR2 catalog (Gaia Collaboration et al. 2018). The large filled red circles and open blue squares show our Kepler and TESS CDGs, respectively. The CDG highlighted with a green circle is HD 91622, which lacks T_{eff} (and carbon abundance) from high-resolution spectra; its T_{eff} was adopted from T. Matsuno et al. (2024). Kernel density histograms are included to show the distributions for various parts of the sample, with the color scheme following the Hertzsprung–Russell diagram, and the dashed histogram showing our CDG sample. Horizontal lines mark CDG luminosity peaks: a solid line at $\log(L/L_\odot) = 1.78$ dex aligns with the core He-burning phase for low-mass stars (i.e., $\log(L/L_\odot) \simeq 1.55$–$1.85$ dex; L. Girardi 2016), and a dashed line at $\log(L/L_\odot) = 2.15$ dex marks the primary peak where most CDGs lie.

systematics in the latter (see Section 4.4.3). Small changes in $\log g$ strongly affect ν_{max} through the scaling relation. A typical uncertainty for the spectroscopic $\log g$ is 0.1 dex. Applying a -0.1 dex offset reduces g by 20.6%, causing an equivalent decrease in ν_{max} for the fixed T_{eff}. For example, for HD 56438, with $\log g = 2.75$ and $T_{eff} = 5037$ K (A. Palacios et al. 2016), this lowers the expected ν_{max} from 67.6 to 53.7 μHz, reducing the residual from the observed 23.0 μHz. Systematic errors, such as those from peculiar abundances (A. Palacios et al. 2016), can further bias $\log g$ and T_{eff}, increasing deviations.

These results suggest that contamination from unresolved companions in binaries likely biases spectroscopic measurements, leading to erroneous predictions for ν_{max}. In summary, agreement between expected and observed ν_{max} is generally good for single CDGs, but breaks down for binaries and multiple systems, where spectroscopic measurements of $\log g$ and/or T_{eff} predict values of ν_{max} that are greater than we observe.

4.4. Determination of Stellar Parameters

4.4.1. Luminosities

Luminosities of the CDGs were determined using the standard formula:

$$\log(L/L_\odot) = -0.4[V_0 - 5\log(d/\mathrm{pc}) + \mathrm{BC} - M_{\mathrm{bol},\odot}]. \quad (3)$$

Distances (d) were taken from the catalog of C. A. L. Bailer-Jones et al. (2021). The visual magnitudes (V_0) and their errors were estimated from the color–color transformations provided in M. Riello et al. (2021), which relate the Gaia DR3 photometric system to the Johnson–Cousins system (P. B. Stetson 2000). We applied bolometric corrections to the absolute magnitudes following the relation from A. Alonso et al. (1999). Reddening values were taken from the 3D dust map of G. M. Green et al. (2019). In cases where the reddening was not available, we took them from the D. J. Schlegel et al. (1998) map, which is recalibrated in E. F. Schlafly & D. P. Finkbeiner (2011). Our derived luminosities are listed in Table 2.

The right panel of Figure 5 shows the Hertzsprung–Russell diagram ($\log(L/L_\odot)$ versus T_{eff}). With the exception of KIC 8352953, the CDGs exhibit luminosities characteristic of RC or EAGB stars. Their luminosity distribution features a primary peak at $\log(L/L_\odot) = 2.15$ dex and a secondary peak at $\log(L/L_\odot) = 1.78$ dex, which correspond to the two luminosity groups in the bimodal distribution reported by S. Maben et al. (2023a), followed by a bright tail extending toward the RGB tip (see also Table 2). The secondary peak aligns with core He-burning predictions for low-mass stars (i.e., $\log(L/L_\odot) \simeq 1.55 - 1.85$ dex; L. Girardi 2016). As shown in S. Maben et al. (2023a; see their Figure 2), 11 of the CDGs have measured asymptotic g-mode period spacings ($\Delta\Pi_1$) and $\Delta\nu$ that place them firmly in the core He-burning RC phase. KIC 8352953, which is also included in the S. Maben et al. (2023a) study and classified as an RGB star by J. Yu et al. (2018), aligns with the lower RGB.

We also include an asteroseismic Hertzsprung–Russell diagram in the left panel of Figure 5. Most CDGs show ν_{max} values lower than typical RC stars, extending to even lower frequencies in the tail, consistent with post-RC evolution, as reflected in the luminosity distribution in the right panel of Figure 5. Notably, the more luminous CDGs ($\log(L/L_\odot) \gtrsim 2.15$ dex) possess higher T_{eff} than typical RGB stars at similar luminosities, reinforcing their interpretation as bright RC or EAGB stars (S. Maben et al. 2023a) rather than RGB stars. This bright tail comprises a mixture of higher-mass CDGs (see Section 4.5.2) and stars that could either be undergoing post-RC evolution toward the EAGB phase, which runs parallel to the RGB and lasts longer than the later stages of the AGB phase, or be massive postmerger core He-burning

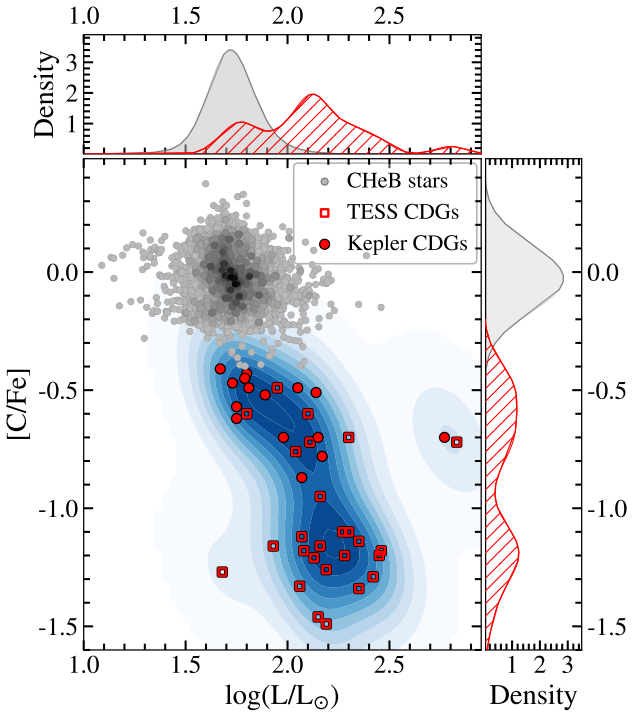

Figure 6. Carbon abundance as a function of $\log(L/L_{\odot})$ for the CDGs (red symbols) with measured $\nu_{\rm max}$, excluding KIC 8352953, a lower-luminosity RGB star, and HD 91622, which lacks carbon abundance measurements from high-resolution spectra. Contours represent the density distribution of CDGs. RC stars from J. Yu et al. (2018; gray circles) form the background, with the color scale indicating the number density of stars (darker colors correspond to higher densities). Kernel density histograms for both CDGs and RC stars are shown along the axes, following the same color scheme. The solar carbon abundance is from N. Grevesse et al. (2007).

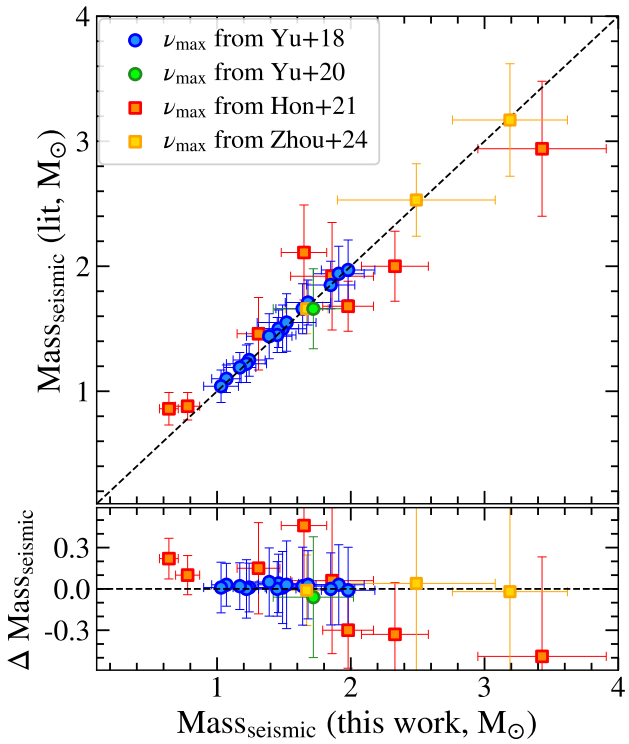

Figure 7. Comparison of seismic masses for 27 CDGs with published $\nu_{\rm max}$ estimates. Masses are derived using $\nu_{\rm max}$ values from this study (via the `pyMON` pipeline) vs. published $\nu_{\rm max}$ values, both calculated with Equation (2). The bottom panel shows star-by-star residuals, expressed in units of $M_{\odot}$. The agreement is excellent, apart from M. Hon et al. (2021; limited data coverage; see Section 4.1).

stars with larger-than-normal helium cores. Only KIC 8352953 exhibits a $T_{\rm eff}$ consistent with the region where RGB stars are typically found, as evident in both panels.

Figure 6 shows carbon abundance versus luminosity for the CDG sample, revealing a clear bimodality in the luminosity distribution. The two groups are centered at $\log(L/L_{\odot}) = 2.0 \pm 0.1$ dex and 2.2 ± 0.1 dex, broadly corresponding to the RC-like and EAGB-like populations in Figure 5. The more luminous group ($\log(L/L_{\odot}) \approx 2.2$ dex) exhibits significantly lower carbon abundances than the fainter group, indicating a carbon–luminosity anticorrelation. This trend is consistent with the results of S. Maben et al. (2023a), who identified a similar bimodality in a smaller sample of 14 CDGs, with peaks at $\log(L/L_{\odot}) = 1.8 \pm 0.1$ dex and 2.1 ± 0.1 dex (see their Figure 3). Our larger sample of 41 stars provides stronger statistical support for this luminosity bimodality. Two CDGs with $\log(L/L_{\odot}) \approx 2.8$ dex, exceeding typical RC or EAGB luminosities, may represent a later, more luminous EAGB phase, or could be merger products with larger He-burning cores.

4.4.2. Masses

Figure 7 compares seismic masses for the 27 CDGs derived from published $\nu_{\rm max}$ measurements (J. Yu et al. 2018, 2020; M. Hon et al. 2021; J. Zhou et al. 2024) with those calculated in this study using $\nu_{\rm max}$ from the `pyMON` pipeline, both determined with Equation (2). Overall, the masses show excellent agreement. Although masses based on $\nu_{\rm max}$ values from M. Hon et al. (2021) are systematically lower by approximately 2.3%, they agree with ours within their respective uncertainties. In contrast, masses derived from $\nu_{\rm max}$ values reported by J. Yu et al. (2018, 2020) and J. Zhou et al. (2024) agree with ours within 1% (see Section 4.1 and Figure 2).

We present the seismic and nonseismic mass determinations for all 43 CDGs in Table 2 and Figure 8. The nonseismic masses were calculated using

$$\left(\frac{M}{M_{\odot}}\right) \simeq \left(\frac{L}{L_{\odot}}\right)\left(\frac{g}{g_{\odot}}\right)\left(\frac{T_{\rm eff}}{T_{\rm eff,\odot}}\right)^{-4}. \quad (4)$$

Figure 8 extends the analysis to our entire CDG sample, comparing individual seismic and nonseismic masses. For Kepler stars, there is good agreement between the two methods for stars with $M \leqslant 2\,M_{\odot}$, as shown in the zoomed inset. For higher-mass stars and those observed by TESS, the seismic and nonseismic methods show disagreement, with nonseismic masses generally exceeding their seismic counterparts.

As discussed in Section 4.4.1, many of our CDGs are luminous giants with $\log(L/L_{\odot}) \gtrsim 2.15$. In this regime, classical asteroseismic scaling relations involving both $\nu_{\rm max}$ and $\Delta\nu$ are known to overestimate masses unless corrected (e.g., with $f_{\Delta\nu}$ factors). However, our mass estimates rely only on $\nu_{\rm max}$, and recent work has shown that the $\nu_{\rm max}$-only scaling relation performs more reliably at high luminosity without requiring such corrections (M. Howell et al. 2024; A. L. Ash et al. 2025).

The mode of the seismic mass distribution for the CDGs is $1.70\,M_{\odot}$ (see top panel of Figure 8), with a spread ranging from $0.61\,M_{\odot}$ to $3.43\,M_{\odot}$. In contrast, the mode of the

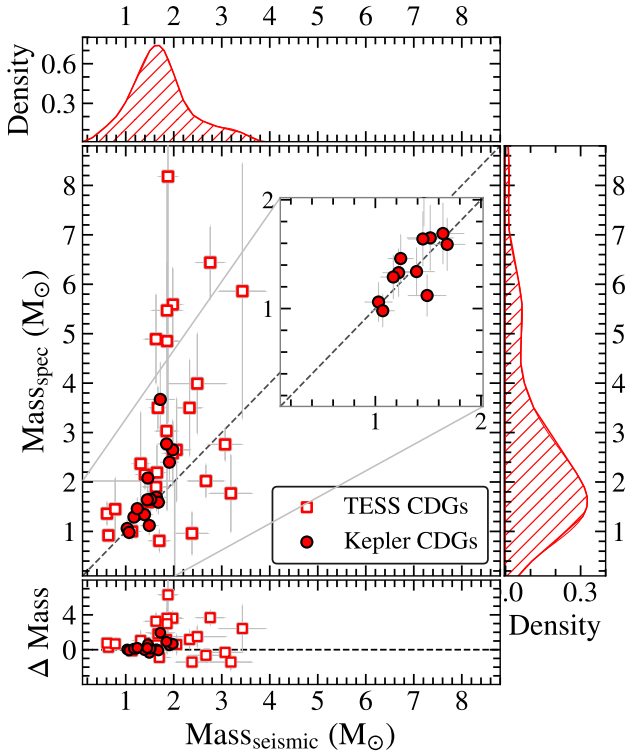

Figure 8. Comparison of seismic masses for the entire seismic CDG sample (43 stars) calculated using Equation (2) with ν_{max} from the `pyMON` pipeline vs. nonseismic masses from Equation (4). The black dashed line again indicates the one-to-one relation, and kernel density histograms show the mass distributions. The zoomed inset highlights Kepler stars. The bottom panel shows star-by-star residuals between nonseismic and seismic masses, expressed in units of $M_\odot$.

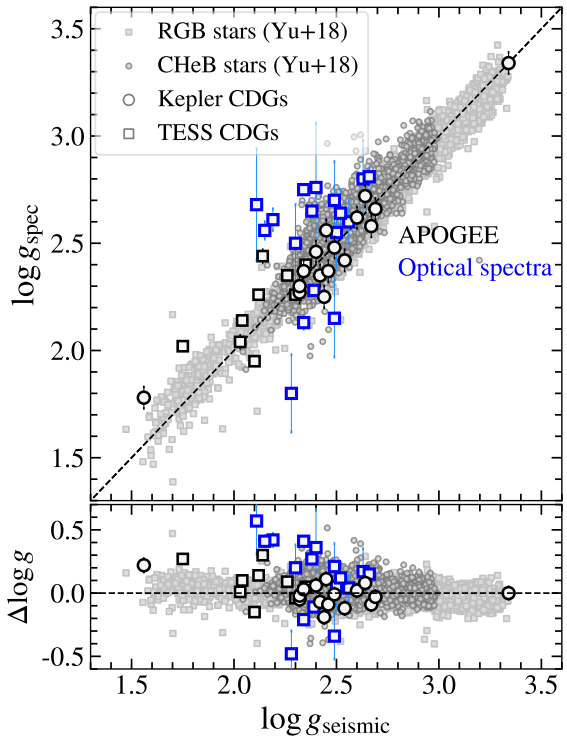

Figure 9. Comparison of seismic surface gravities using ν_{max} values from this study vs. spectroscopic surface gravities for CDGs from literature, excluding HD 91622, since it lacks spectroscopic log g measurement. Background RGB and RC stars from J. Yu et al. (2018) use spectroscopic log g from APOGEE DR17, with seismic log g derived using J. Yu et al. (2018) ν_{max} and APOGEE DR17 T_{eff}. The black dashed line denotes the one-to-one relation. CDGs with spectroscopic log g from APOGEE DR17 (black) and optical spectra (blue) are also shown. The bottom panel shows star-by-star residuals between spectroscopic and seismic log g.

nonseismic mass distribution is 1.59 $M_\odot$ (see right panel of Figure 8), with a broader spread from 0.81 $M_\odot$ to 8.18 $M_\odot$. While both mass distributions peak at similar values, the seismic masses exhibit a much narrower spread. This difference is also reflected in the typical uncertainties: the mean uncertainty for the seismic masses is 0.21 $M_\odot$, whereas for the nonseismic masses it is substantially larger at 0.67 $M_\odot$.

4.4.3. Seismic Surface Gravities

We estimated the seismic surface gravities of the CDGs using the scaling relation:

$$\left(\frac{g}{g_\odot}\right) \simeq \left(\frac{\nu_{max}}{\nu_{max,\odot}}\right)\left(\frac{T_{eff}}{T_{eff,\odot}}\right)^{-1/2}. \quad (5)$$

Asteroseismic log g uncertainties average $\pm$0.01 dex, far lower than spectroscopic log g uncertainties of $\pm$0.07 dex from high-resolution spectra. The offset between the spectroscopic and seismic log g is

$$\log g_{spec} - \log g_{seis} = 0.06 \pm 0.22 \text{ dex},$$

which is consistent with zero within the uncertainties. However, as discussed in Section 4.3, standard solar-scaled models can yield incorrect spectroscopic log g values for CDGs due to their peculiar chemistry (A. Palacios et al. 2016).

Figure 9 compares these values, showing the spectroscopic log g from APOGEE DR17 and optical spectra against seismic log g, with RGB and RC stars from J. Yu et al. (2018) as background. The systematic offsets are quantitatively smaller for APOGEE-derived measurements (0.02 $\pm$ 0.12 dex) than optical spectra (0.13 $\pm$ 0.28 dex), due to the application of a neural network-based calibration in APOGEE that incorporates asteroseismic parameters (J. A. Holtzman et al. 2018; Abdurro'uf et al. 2022). For J. Yu et al. (2018) giants, the spectroscopic log g exceeds seismic values at lower log g, especially for RC stars, consistent with APOGEE trends (M. H. Pinsonneault et al. 2014). These differences further support our analysis in Section 4.3 regarding the challenges in spectroscopic log g determinations for giants (T. Masseron & K. Hawkins 2017). The superior accuracy of seismic log g determinations significantly enhances the reliability of evolutionary classifications.

4.5. Characterization of Carbon-deficient Stars

4.5.1. Three Groups of CDGs

In the previous study of 15 Kepler field CDGs (S. Maben et al. 2023a), 14 were RC stars. Based on available data, we divided them into two groups based on their luminosity and chemical patterns: Group 1 CDGs (normal-luminosity RC stars; eight stars); and Group 2 CDGs (overluminous RC stars; six stars). The remaining CDG was an RGB star. We also compared these CDGs to 29 previously known wGb stars, and also assigned them to groups, based on their chemistry and luminosities: Group 3a (6 wGb stars) and Group 3b (23 wGb stars). Group 3a consisted of primarily low-mass stars, with limited seismic data from TESS, but which appeared

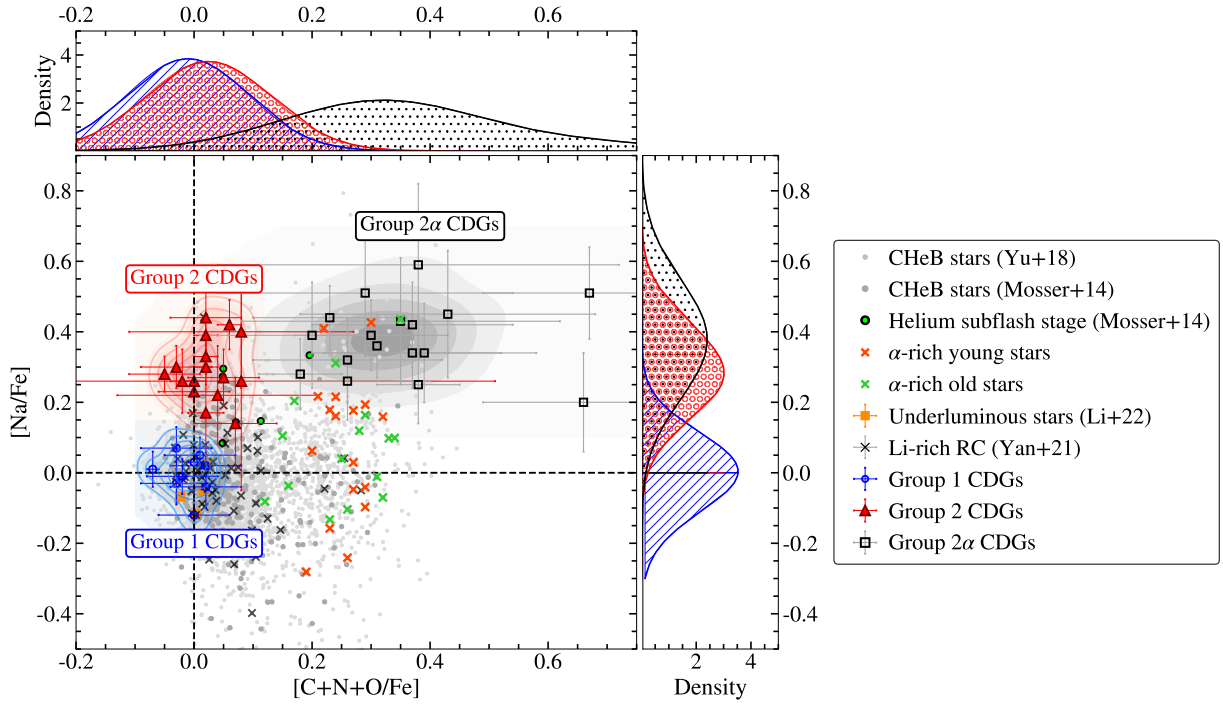

Figure 10. Trends of sodium abundance vs. the [C+N+O/Fe] abundance ratio. Giants classified based on asteroseismic analysis form the background from B. Mosser et al. (2014) and J. Yu et al. (2018; small filled circles; see key). The underluminous stars from Y. Li et al. (2022) are shown by orange squares. The abundance ratios of the normal giants and the underluminous stars are from APOGEE DR17. The Group 1, Group 2, and Group 2α CDGs are represented by blue circles, red triangles, and black squares, respectively. The Li-rich giants (black crosses) are from the H.-L. Yan et al. (2021) study. These Li-rich giants are the low-spectral-resolution RC sample that had good-quality APOGEE DR17 data (59 stars). The α-rich young (orange crosses) and old stars (green crosses) were compiled by S. Hekker & J. A. Johnson (2019) from the P. Jofré et al. (2016) and M. H. Pinsonneault et al. (2018) studies. Solar abundances are from N. Grevesse et al. (2007). Contours highlight the separation into three groups based on their Na and CNO abundances.

overluminous for their masses and showed evidence of more extreme chemical pollution as compared to Groups 1 and 2. Group 3b were wGb stars without any seismic data, which also showed extreme chemical pollution but lacked seismic mass constraints.

In this study, our sample with seismic data (43 CDGs) is approximately 3 times the size of the previous sample. In this sample, we find that, while there is a clear progression from lower to higher luminosities between the groups, a significant overlap in luminosity among the CDGs makes it challenging to define distinct groups based solely on this parameter (see Figures 5 and 6). A clearer distinction emerges in the [Na/Fe] versus [C+N+O/Fe] abundance plane (see Figure 10). Here, the CDGs separate into three distinct groups based on their chemical abundances:

1. Group 1 CDGs, normal [Na/Fe] abundances with scaled-solar [C+N+O/Fe] compositions;
2. Group 2 CDGs, enhanced [Na/Fe] abundances, also with scaled-solar [C+N+O/Fe] compositions;
3. Group 2α CDGs, enhanced in both [Na/Fe] and [C+N+O/Fe], with an average [C+N+O/Fe] enhancement of +0.4 dex; this group aligns with the previously identified wGb stars, reinforcing its distinct nature.

The naming of the third group as 2α is based on further inspection, which indicates that it is very similar to Group 2, as we describe below.

4.5.2. Deciphering Group 2α

In Table 3, we collate and summarize all available information from the current study, including atmospheric parameters, abundances, masses, and luminosities. Here, we see that Groups 1 and 2 are quite distinct, with effective temperatures, luminosities, and masses increasing between them. Chemical abundances also show progressively higher [Na/Fe], greater [C/Fe] depletion, and a decreasing [C/N] ratio. The differences between these groups suggest distinct formation pathways.

On the other hand, comparing Group 2 and Group 2α, we see that their surface temperatures and seismic $\log g$ are very

Table 3
Comparison of CDG Classifications

	Group 1	Group 2	Group 2α
$T_{\rm eff}$ (K)	4840	5000	5050
$\log g_{\rm seismic}$	2.5	2.4	2.4
Lum. ($L_\odot$)	61	116	143
Mass ($M_\odot$)	1.2	1.7	1.9
[Na/Fe]	0.0	+0.3	+0.4
[CNO/Fe]	0.0	0.0	+0.3
Li-rich frac.	67%–100%	38%–94%	53%–59%
[C/Fe]	−0.5	−0.7	−1.2
[N/Fe]	+0.6	+0.7	+1.2
[O/Fe]	0.0	0.0	+0.2
[C/N]	−1.0	−1.4	−2.4
$^{12}C/^{13}C$	…	5	4
[Fe/H]	−0.1	−0.1	−0.2

Note. Approximate modes are given for each parameter. Li-rich fractions are ranges, with lower bounds from measured Li-rich stars only and upper bounds assuming all unmeasured stars are Li rich. Ellipses indicate unavailable data.

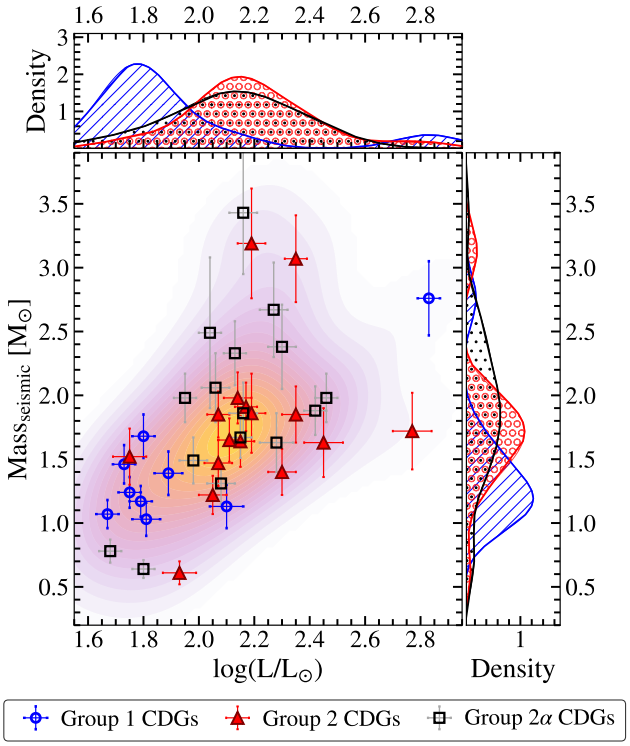

Figure 11. Seismic mass vs. $\log(L/L_\odot)$ for CDGs, with Group 1, Group 2, and Group 2α shown as blue circles, red triangles, and black squares, respectively. Kernel density histograms illustrate the distributions for each group, using the corresponding group colors. Contours represent the density distribution of the full sample.

similar. As mentioned above, luminosity is not a good discriminator between the groups, since there is an overlap in luminosity distributions (see Figure 11). Allowing for uncertainties, their masses, [Fe/H], [Na/Fe], $^{12}C/^{13}C$, and Li-rich fraction are also similar. Where Groups 2 and 2α diverge significantly is in their CNO abundances. Group 2α has, on average, a much more extreme [C/Fe] depletion. This could be due to more thorough burning through the CN cycle. Although this suggests higher average [N/Fe] abundances—which are observed—the abundances are much higher than would be expected (+0.5 dex greater than the other groups). To illustrate this, in Figure 12, we show an estimate for the highest [N/Fe] expected from a CN burn (vertical gray shading; assuming complete burning from initially scaled-solar composition). The majority of the Group 2α stars are found to have values greater than this upper limit, while the Group 2 CDGs are consistent with being at or below it. Looking at the distribution of [C/Fe] in Figure 12, we see that each distribution has (essentially the same) two peaks, and that there is a complete overlap between these two groups. The [C/Fe] averages are so different (Table 3) because Group 2α has more members in the peak around [C/Fe] ~ -1.25 dex, than the peak around 0.7 dex. Apart from this, the range and peak locations of the distributions are essentially the same. This begs the question as to why the Group 2α CDGs have such high [N/Fe] when their [C/Fe] is similar to ~40% of Group 2 CDGs. The similarity of the [C/Fe] distributions to Group 2 suggests that Group 2α has not*not* undergone more thorough burning through the CN cycle, reinforcing that N is particularly overabundant in these CDGs.

Turning to other elements, we see that Group 2α has an overabundance of [O/Fe]. Overabundances of [O/Fe] between 0.2 and 0.5 dex are reminiscent of α-enhanced stars. To check this, we analyzed other α element abundances for the sample. As an example, in Figure 13, we show [Mg/Fe] for all three groups, along with a background sample of Galactic giants, and dedicated literature samples of α-rich and α-normal stars. From this figure, it is clear that the Group 2α stars can be associated with the α-rich thick-disk population of the Galaxy (this is also seen in Ti), while the Group 2 (and Group 1) stars are predominantly α-normal, following the thin-disk composition. This strongly suggests that Group 2α CDGs formed from a thick-disk-like initial composition, and that CN burning on this abundance pattern has led to the unusually high N. We checked this quantitatively by assuming that (i) no ON cycling had occurred (so the current [O/Fe] is the same as the initial), (ii) the initial [N/Fe] was scaled-solar (as seen in observations of α-rich stars), and (iii) the current [C+N+O/Fe] has not changed from the initial value. This gives an enhanced initial [C/Fe], which, when burned through the CN cycle, results in high N abundances, since C is much more abundant than N. Using this method on a star-by-star basis, we matched almost all of the [N/Fe] values currently observed in the Group 2α CDGs. Since all other parameters are essentially the same as Group 2 (allowing for some uncertainties), we conclude that Group 2α CDGs are just α-rich counterparts of the Group 2 CDGs. That is, their origin is very likely to have been the same; they just formed with a different composition—hence the name Group 2α. This interpretation is different to that in S. Maben et al. (2023a)—where they concluded that some dredge-up from the core had enhanced the O—because our current data set is much larger and more detailed. This finding reduces the complexity of the CDGs, suggesting that one less formation scenario is required.

4.5.3. Further Analysis of Chemical Patterns of the Three Groups

As noted above, Groups 1 and 2 have [C+N+O/Fe] = 0.0, reflecting CN cycling without detectable enrichment (G. R. Caughlan 1965). With our new analysis of Group 2α showing that those CDGs have different initial compositions, it is now clear that Group 2α also only underwent CN cycling, and no ON cycling. As pointed out by S. Maben et al. (2023a), Group 1's [Na/Fe] = 0.0 indicates moderate-temperature burning (20–40 MK; J. Adamczak & D. L. Lambert 2013), and Group 2's [Na/Fe] = +0.3, with [C/Fe] = −0.7, [N/Fe] = +0.7, [O/Fe] = 0.0, suggests hotter conditions (50–60 MK). The sodium abundance in Group 2α is very similar, and, as discussed above, only CN cycling has occurred, suggesting these CDGs underwent burning at about the same temperature as Group 2.

We have $^{12}C/^{13}C$ ratios for 16 of the 42 CDGs from the literature. The modes of the ratio distributions for Group 2 and Group 2α are given in Table 3 (we have no data for Group 1 stars). Both values are low, 4–5, supporting advanced CN cycling, consistent with the [C/N] values (J. A. Brown et al. 1989).

To further probe stellar processing, we analyze lithium abundances, for which we have measurements for 29 of the 42 CDGs (Table 3). All six of six Group 1 stars with Li measurements are found to be Li rich (A(Li) > 1.5 dex), giving a Li-rich fraction of 67%–100% (three stars have no measurements). For Group 2, 6 of 7 stars are Li rich (38%–94%, 9 stars

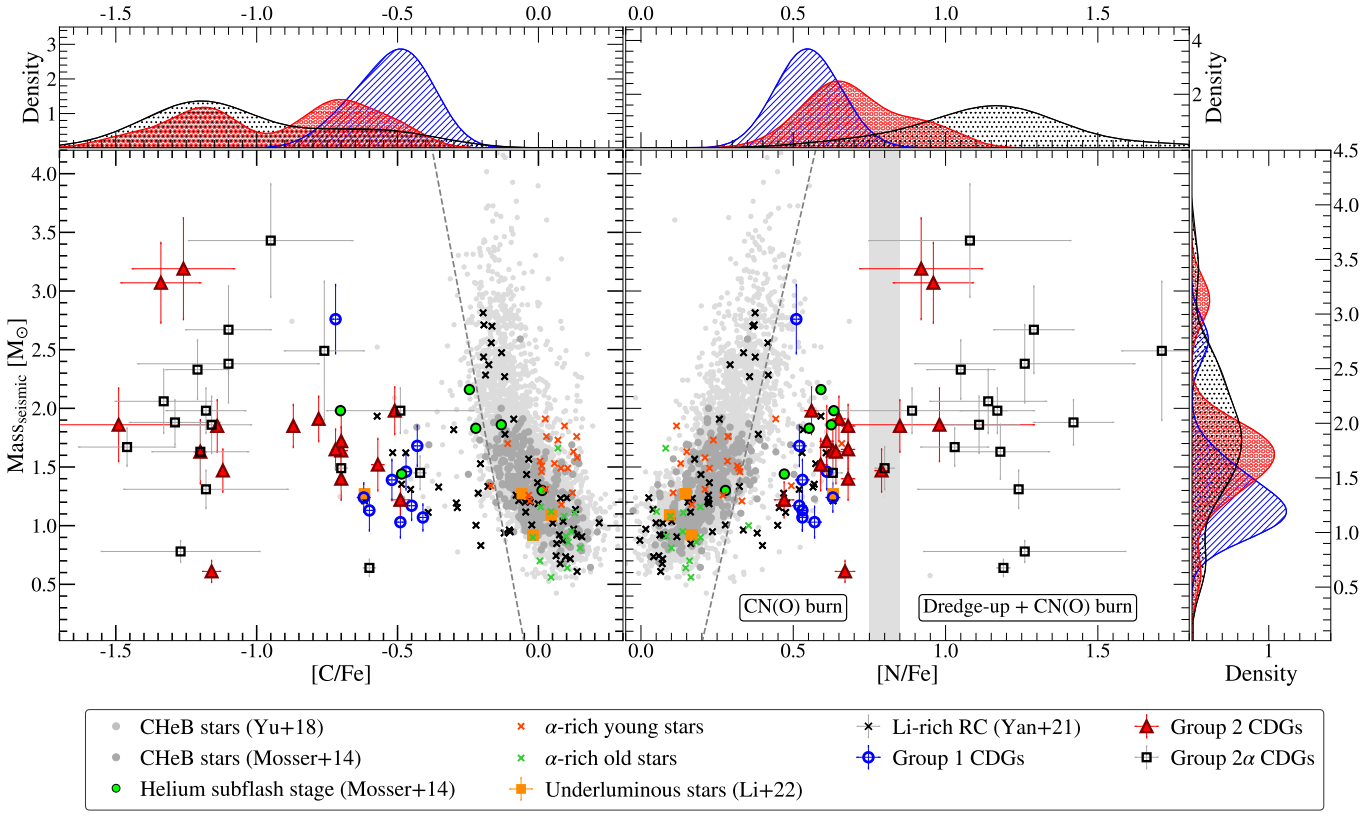

Figure 12. Seismic mass vs. [C/Fe] (left panel) and vs. [N/Fe] (right panel) for the CDGs, underluminous stars, Li-rich giants, α-rich stars, and a large sample of RC stars with symbols having the same meaning as in Figure 10. We determine luminosities for the Li-rich giants in the same manner as our CDGs. Using this, we estimated the seismic masses of these stars using mass from Equation (2). The "normal" RC stars show a correlation between mass and nitrogen (and carbon) abundance. This reflects first dredge-up surface pollution from early on the RGB (e.g., I. Iben & A. Renzini 1984). The trend shows fairly sharp edges, allowing us to make a cut in N (or C) that varies with mass (dashed lines). This helps in distinguishing the chemically peculiar stars. To the right of the N line, the stars can be considered N rich, for their mass. The vertical shaded region at [N/Fe] $= +0.8 \pm 0.05$ dex denotes the upper limit of our CDG sample's N enhancement as well as the highest N abundance possible for scaled-solar composition, if the ON cycle was activated after all C is burned to N. Solar abundances are from N. Grevesse et al. (2007).

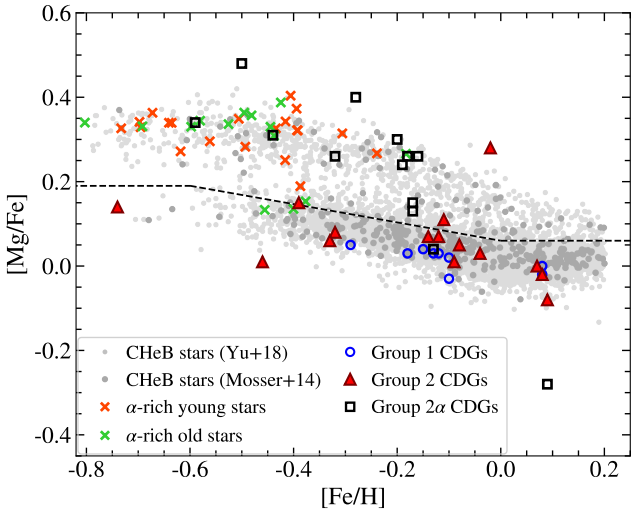

Figure 13. [Mg/Fe] ratio as a function of [Fe/H]. Giants classified based on asteroseismic analysis form the background from B. Mosser et al. (2014) and J. Yu et al. (2018; small filled circles; see key). The α-rich young (orange crosses) and old stars (green crosses) are compiled by S. Hekker & J. A. Johnson (2019). Both the normal giants and these α-rich stars have abundance ratios from APOGEE DR17. The Group 1, Group 2, and Group 2α CDGs are represented by blue circles, red triangles, and black squares, respectively. The black dashed line shows the separation between thin- and thick-disk stars based on the [Mg/Fe] ratio, similar to V. Z. Adibekyan et al. (2011).

without measurements), and for Group 2α, 9 of 16 stars are Li rich (53%–59%, 1 star with no measurement). These very high rates of Li-richness, despite high burning temperatures, point to mixing in the event(s) that formed the chemical patterns of the CDGs.

This prevalence of Li-rich giants is particularly remarkable given that, during the first dredge-up on the RGB, convective mixing dramatically reduces the surface lithium abundance—A(Li) typically drops by about 95% from its main-sequence (MS) value (I. Iben 1967). As a result, Li-rich giants are extremely rare in the field, representing only about 1% of giants (J. A. Brown et al. 1989; S. L. Martell & M. D. Shetrone 2013; A. R. Casey et al. 2019; Y. B. Kumar et al. 2020). The exceptionally high Li-rich fractions found in all three CDG groups thus stand in stark contrast to this general rarity, highlighting the unusual nature of these stars and the importance of internal mixing or nonstandard processes in shaping their chemical compositions.

Finally, we note that pollution from AGB stars as a source of the abundance patterns of CDGs is unlikely given that [C+N+O] appears to be unchanged in all groups, while [C+N+O] increases with the third dredge-up in thermally pulsing AGB (TP-AGB) stars (e.g., A. I. Karakas & J. C. Lattanzio 2014).

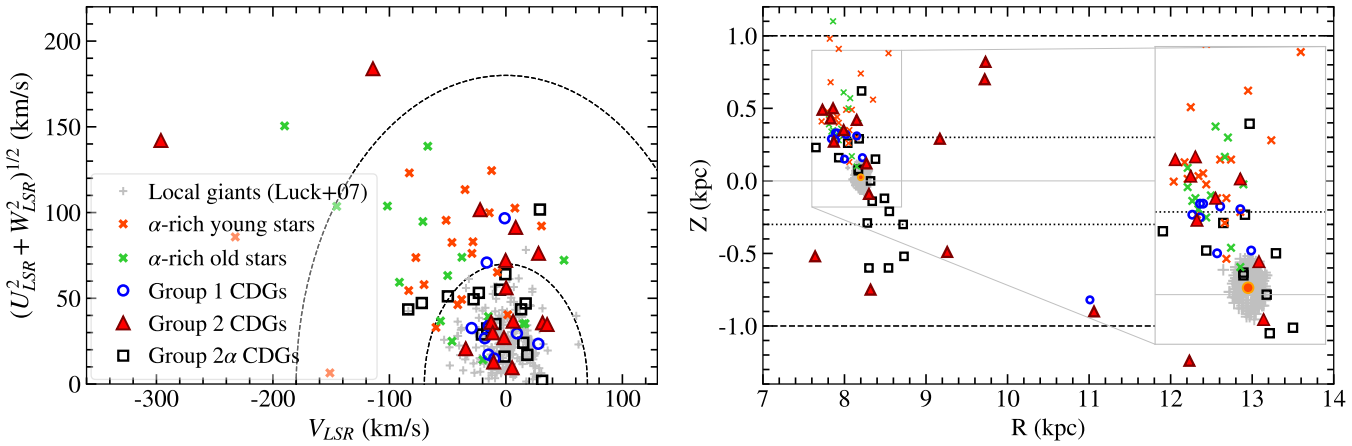

Figure 14. Left panel: the three groups of CDGs, including α-rich young and old stars compiled by S. Hekker & J. A. Johnson (2019) and local giants from R. E. Luck & U. Heiter (2007), are shown in the Toomre diagram. Dashed lines show constant values of the total space velocity, $v_{\rm tot} = (U_{\rm LSR}^2+V_{\rm LSR}^2+W_{\rm LSR}^2)^{1/2}$ at 70 and 180 km s^{-1}, demarcating thin-disk and thick-disk components, respectively (Nissen et al. 2004; K. A. Venn et al. 2004). Right panel: spatial distribution above/below the Galactic plane vs. the galactocentric distance. The commonly accepted scale heights of the thin disk and thick disk are indicated at $Z = \pm$ 0.3 kpc (dotted lines) and $Z = \pm$1 kpc (dashed lines), respectively (L. S. Sparke & J. S. I. Gallagher 2007). The Sun (filled yellow circle) is at R = 8.2 kpc and Z = 0.025 kpc.

4.5.4. Kinematics and Galactic Component Membership

Following S. Maben et al. (2023a), we analyzed CDG kinematics using Astropy's `Galactocentric` module (Astropy Collaboration et al. 2013, 2018), with distances (C. A. L. Bailer-Jones et al. 2021), Gaia DR3 proper motions (Gaia Collaboration et al. 2016; Gaia Collaboration 2022), and radial velocities from literature (J. Adamczak & D. L. Lambert 2013; A. Palacios et al. 2016; N. Holanda et al. 2023, 2024; S. Maben et al. 2023a, 2023b) and R. E. Luck & U. Heiter (2007) for the CDGs and local giants, respectively. We categorize stars with $v_{\rm tot} < 70$ km s^{-1} as thin-disk stars, those between 70 and 180 km s^{-1} as thick-disk stars, and those with velocities greater than this as halo stars (P.E. Nissen 2004; K. A. Venn et al. 2004).

The Toomre diagram, shown in the left panel of Figure 14, reveals that 78% of Group 1 CDGs belong to the thin disk, with two CDGs classified as thick-disk members. For Group 2, 63% of the CDGs are thin-disk members, four CDGs are thick-disk members, and two CDGs belong to the halo population. Group 2α CDGs are 76% thin-disk members, while four CDGs belong to the thick disk. Interestingly, old thin-disk stars with enhanced [α/Fe] at similar [Fe/H] share kinematic properties with Group 2α CDGs (S. Nepal et al. 2024). Despite exhibiting high [α/Fe] ratios typical of the thick disk, the kinematics of Group 2α CDGs indicate that they predominantly occupy thin-disk orbits.

Overall, our kinematic analysis shows that approximately 72% of the CDGs belong to the thin disk, 23% belong to the thick disk, and 5% belong to the halo. The magnitude-limited nature of our sample favors nearby thin-disk stars, likely influenced by dynamical mixing near the thin-disk–thick-disk boundary. The spatial distribution in the R–Z plane (see right panel of Figure 14) further illustrates the spread expected from dynamical evolution (L. S. Sparke & J. S. I. Gallagher 2007; H. E. Bond 2019).

Although chemically peculiar, the kinematics of the CDGs provide valuable insights into the dynamical history of the Milky Way's disk and its distinct stellar populations.

4.6. Formation Scenarios for CDGs

The formation mechanisms of CDGs remain a subject of active investigation. S. Maben et al. (2023a) identified three groups of CDGs based on their luminosity and chemical properties: (i) normal-luminosity RC CDGs, (ii) overluminous RC CDGs, and (iii) overluminous, highly polluted CDGs (previously known as wGb stars). They found that mergers between HeWDs and RGB stars were the most likely formation pathway for the two overluminous groups, while binary mass transfer from intermediate-mass AGB stars remained a viable scenario for the highly polluted subset. For the normal-luminosity CDGs, they could not distinguish between pollution from the core He-flash and lower-mass merger events with the available data.

With the expanded CDG sample and improved asteroseismic constraints available in this study, we are now positioned to reassess the formation pathways previously proposed for the CDG groups. We evaluate the plausibility of each scenario in light of the updated seismic, photometric, and abundance information.

The $\log(L/L_{\odot}) - \nu_{\rm max}$ diagram (Figure 15) serves as a useful diagnostic. When comparing the CDGs with the broader RC and RGB populations in this plane, we see that the distribution of CDGs shows deviations from standard evolutionary sequences, offering insight into their formation histories.

4.6.1. Group 1: Core–Flash Mixing or Low-mass Mergers?

Group 1 CDGs display luminosities and seismic parameters consistent with core He-burning RC stars. For the majority of these stars, both $\Delta\Pi_1$ and $\Delta\nu$ are measured. Specifically, seven out of nine Group 1 stars have both parameters available (B. Mosser et al. 2014; M. Vrard et al. 2016; S. Maben et al. 2023a)—firmly establishing their evolutionary status. In Figure 15, Group 1 stars overlap with the region occupied by the general RC population in both luminosity and $\nu_{\rm max}$, further supporting their classification as low-mass core He-burning giants.

Chemically, Group 1 stars show moderate carbon depletion and nitrogen enhancement, with [C+N+O/Fe] remaining near

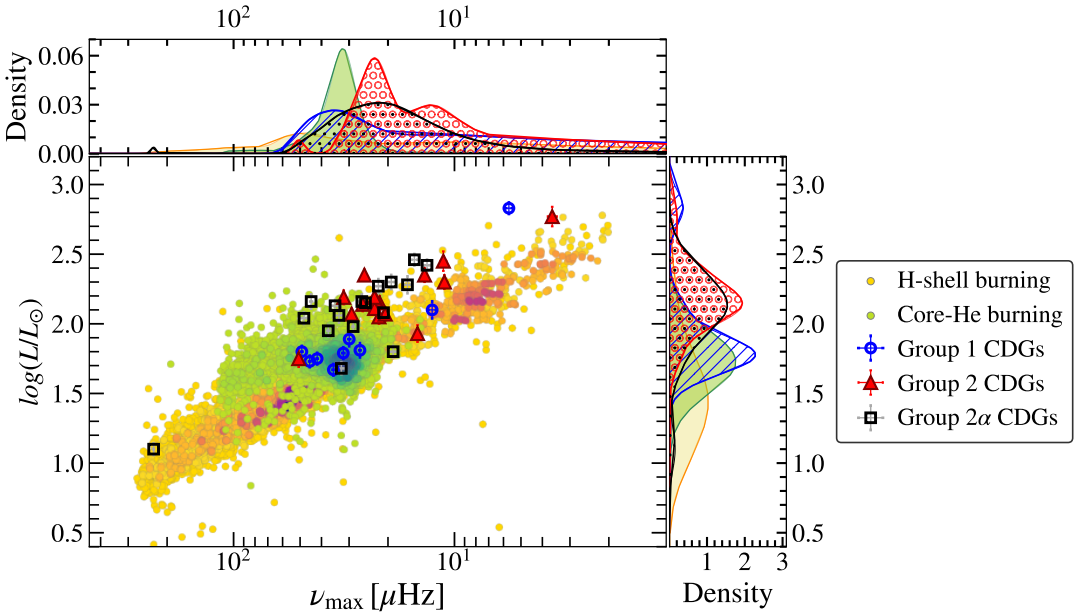

Figure 15. $\log(L/L_{\odot})$ is shown as a function of $\nu_{\max}$ for CDGs. Group 1, Group 2, and Group 2α stars are indicated by blue circles, red triangles, and black squares, respectively. RGB stars (yellow circles) and He-core burning giants (green circles) from M. H. Pinsonneault et al. (2018) and J. Yu et al. (2018) form the background, with the color scale representing the number density of stars (darker colors indicate higher density). Kernel density histograms for each group are shown along the axes, following the same color scheme.

solar. Their sodium abundances are approximately solar ([Na/Fe] $\approx$ 0.0), consistent with CN cycling at moderate temperatures ($\simeq$20–40 MK) without activation of the Ne–Na cycle (J. Adamczak & D. L. Lambert 2013). This pattern suggests internal envelope mixing with moderate burning rather than deep, high-temperature nucleosynthesis.

A striking feature of Group 1 is the exceptionally high fraction of Li-rich stars: all six stars with lithium measurements are Li rich (A(Li) $>$ 1.5 dex), in stark contrast to the field giant population, where such stars are very rare (e.g., J. A. Brown et al. 1989; S. L. Martell & M. D. Shetrone 2013; A. R. Casey et al. 2019; Y. B. Kumar et al. 2020). Such enrichment is consistent with in-situ lithium production near the RGB tip, as proposed for low-mass RC stars by Y. B. Kumar et al. (2020).

The luminosity distribution and mass range of Group 1 stars further constrain the nature of the mixing processes responsible for their chemical peculiarities. The fact that CDGs are generally not observed at luminosities below the RC (see Figures 5 and 15) suggests that the pollution or mixing event responsible for their chemical peculiarities occurs near the RGB tip, as also noted by S. Maben et al. (2023a). Given the mass range of Group 1 stars—eight out of nine stars lie between 1.03 $M_{\odot}$ and 1.68 $M_{\odot}$—these stars are expected to have experienced degenerate helium ignition in their cores, i.e., the core He-flash. While previous studies have suggested that envelope pollution during the core He-flash could increase surface carbon (e.g., R. G. Deupree & R. K. Wallace 1987; R. G. Izzard et al. 2007; M. Mocák et al. 2009), such carbon enhancement is incompatible with the carbon-deficient nature of Group 1 stars. Instead, the mild in-situ mixing event at the core He-flash, which was proposed to explain Li-rich giants (Y. B. Kumar et al. 2011, 2020; S. Maben et al. 2023a; also see modeling by J. Schwab 2020; K. Mori et al. 2021), was extended by S. Maben et al. (2023a) to include a regime of intermediate flash-induced mixing in which partial CN(O) burning enhances nitrogen and depletes carbon without affecting sodium or total [C+N+O]—matching the Group 1 CDG chemical patterns. To date, such a mixing regime has not been fully explored in stellar models.

While internal mixing remains a plausible explanation, external pollution scenarios must also be considered. In particular, mass transfer from an AGB companion would increase [C+N+O/Fe], which is not observed (see Section 4.5.3), so AGB mass transfer is precluded. The Group 1 CDG chemical patterns could still have come from a different type of binary companion (although we struggle to find candidates). Binary information would help in exploring this possibility; however, only one Group 1 star is currently identified as a binary, corresponding to a binary fraction of $\sim$11%. However, this likely represents a lower limit due to observational incompleteness. At present, the available binary data are insufficient to conclusively favor or rule out any binary formation pathway.

The mass distribution of Group 1 is very similar to the general RC population, with the same peak at 1.2 $M_{\odot}$ (Table 3). The absence of a bias to higher-mass stars, and the absence of a high-mass tail, disfavors a merger origin for this group. However, given the limited sample size, this conclusion remains tentative.

In summary, Group 1 CDGs are low-mass RC stars exhibiting lithium enrichment and mild CN processing without sodium enhancement. Their properties are best explained by in-situ mixing associated with the core He-flash, consistent with theoretical scenarios proposed by Y. B. Kumar et al. (2011, 2020), J. Schwab (2020), and S. Maben et al. (2023a). The absence of carbon enhancement and [C+N+O] enrichment argues against AGB mass transfer, and the lack of a mass bias and high-mass tail makes mergers less likely. This contrasts with Group 2 CDGs, which are more massive, sodium rich, and likely require a merger origin (Section 4.6.2). More complete binary surveys and larger samples will be essential to confirm the dominant formation mechanism for Group 1.

4.6.2. Groups 2 and 2α: He Subflashes, AGB Mass Transfer, or More Massive Mergers?

As discussed in Section 4.5.2, we now consider the Group 3 stars of S. Maben et al. (2023a) as α-enhanced analogs of Group 2. This simplifies the analysis of the CDGs since we are now essentially only dealing with two groups. As reported in S. Maben et al. (2023a), Group 2 CDGs are clearly more luminous and more massive than normal RC stars (also see Table 3). They also show more advanced burning as compared to Group 1, with enhanced Na and lower [C/N]. Although [C/Fe] and [N/Fe] are different between Groups 2 and 2α, we determined in Section 4.5.2 that this is solely due to their different initial compositions.

Only a few stars in each group have both $\Delta\Pi_1$ and $\Delta\nu$ measurements available from the literature (B. Mosser et al. 2014; M. Vrard et al. 2016; J. Yu et al. 2018), specifically 3 out of 16 Group 2 stars and 1 out of 17 Group 2α stars. For these stars, the seismic values are consistent with core He-burning RC evolution. Two of the Group 2 CDGs are classified as helium subflashing stars by B. Mosser et al. (2014). Subflashes occur during a brief phase leading up the main core He-flash. In the $\nu_{\rm max}$–log L plane, the majority of Group 2 and Group 2α stars form an offset sequence at higher luminosity (lower $\nu_{\rm max}$) than normal RC stars of the same seismic mass, matching the "overluminous" RC component seen in previous studies.

These observational patterns naturally raise the question of whether existing theoretical merger models can explain the properties of Group 2 and 2α CDGs. For comparison, N. Z. Rui & J. Fuller (2021) focused on mergers involving MS and RGB stars, which produce RGB remnants with overmassive envelopes, smaller $\Delta\Pi_1$, and lower luminosities than single stars of comparable mass. These remnants are not RC stars and thus do not resemble the "overluminous" RC CDGs observed here. This indicates that Groups 2 and 2α likely formed through a different merger channel, such as HeWD–RGB core mergers that increase the He-core mass (S. Maben et al. 2023a).

A key new result from our expanded sample is that AGB pollution can now be clearly ruled out as a formation pathway for both Groups 2 and 2α. In all cases, [C+N+O] remains unchanged from the stars' initial values (see analysis of Group 2α in Section 4.5.2), while the third dredge-up in TP-AGB stars increases the total CNO abundance through the mixing up of the intershell material, which is rich in C (e.g., A. I. Karakas & J. C. Lattanzio 2014). There is also no evidence for an unusually high binary fraction in Group 2: only 2 out of 16 stars (12.5%) are reported as binaries in the literature. Due to data limitations, this is only a lower limit, but if it were to hold for the whole group, it would further argue against an AGB mass-transfer origin. In contrast, Group 2α stands out with quite a high binary fraction: 10 out of 17 stars (59%) are reported as binaries in the literature. This suggests that binary interactions or mergers are especially important in the evolutionary history of Group 2α CDGs.

Of the 10 Group 2α CDGs identified as binaries, five have both angular separation (ρ) and distance (d) measurements available in the literature, allowing us to estimate their orbital separations (Table 4). The projected separation a_p was calculated as

$$a_p = \rho \times d, \tag{6}$$

where ρ is in arcseconds, and d is in parsecs, yielding a_p in au (J. B. Holberg et al. 2013). To convert this projected quantity into a physical orbital separation, information on the orbital eccentricity and inclination is required—but these parameters are not available for our systems. As such, we adopt a statistical approach. T. J. Dupuy & M. C. Liu (2011) use Monte Carlo simulations to compute distributions of correction factors that convert projected separations into semimajor axes, averaging over orbital orientations and eccentricities. From their Table C1, we adopt the median correction factor of 1.10, appropriate for systems with uniform eccentricity distributions and no discovery bias. The orbital separation is then estimated as

$$\hat{a} = 1.10 \times a_p. \tag{7}$$

Table 4
Estimated Orbital Separations for Group 2α CDGs

Star	ρ (arcsec)	d (pc)	a_p (au)	$\hat{a}$ (au)
HD 91805	17.80[a]	251.23	4471.99	4919.19
HD 40402	12.40[a]	597.89	7413.90	8155.29
HD 18636	20.78[b]	361.45	7511.04	8262.14
HD 49960	12.70[a]	592.43	7523.89	8276.28
HD 124721	47.23[b]	789.54	37,290.19	41,019.21

Notes.
[a] B. D. Mason et al. (2001).
[b] K. El-Badry et al. (2021).

All five stars with available orbital data are found to be very wide binaries (∼5000–40,000 au; Table 4).

To examine whether CDGs have different orbital properties compared to normal field stars, we recreated the binary separation distributions from R. J. Parker & M. R. Meyer (2014; see their Figure 1) and placed the estimated orbital separations of our Group 2α CDG binaries on the plot (Figure 16). The CDG binaries appear mostly at the (very) wide end of the separation range. This might suggest that these stars prefer very wide binaries. However, the current data are likely biased toward detecting wide binaries, so we cannot draw firm conclusions. Based on available data, 5/17 (29%) of Group 2α CDGs are very wide binaries, which gives us a lower limit on the wide binary fraction. This could still be consistent with normal binary populations, but more data are needed to be sure.

The overall binary fraction should also be considered. Our sample shows a 59% binary fraction for Group 2α CDGs. If this includes both close and wide binaries, the value may be directly comparable to the overall binary fraction in the field. But if the detections are mostly sensitive to wide binaries (as with the five systems above), the 59% should be compared to the very wide binary fraction, in which case it is very high compared to that observed in field stars (e.g., R. J. De Rosa et al. 2014; R. J. Parker & M. R. Meyer 2014). That is, the Group 2α binary fraction would appear to be elevated. Only a dedicated binarity study can definitively tell us the true separation distribution, so this is an important topic for future work.

These wide CDG binaries can be explained if these stars arise from hierarchical triple systems. In this case, the inner two stars merge to form the CDG, while the third star remains in a wide orbit, with the system then identified as a wide

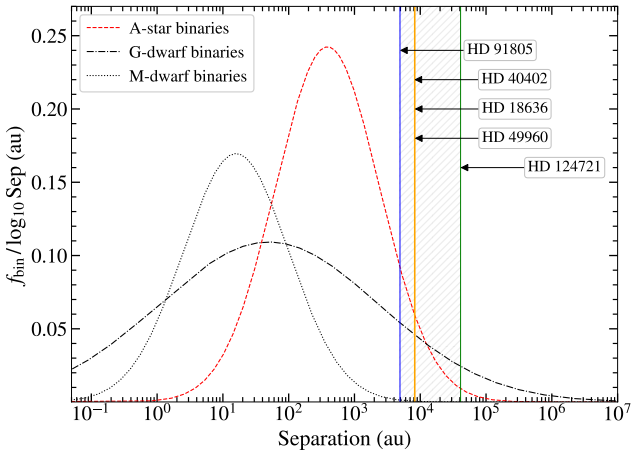

Figure 16. Log-normal fits to binary separation distributions in the Galactic field, following R. J. Parker & M. R. Meyer (2014). The fit to A-star binaries (red dashed) is from R. J. De Rosa et al. (2014), G-dwarfs (black dashed–dotted) from D. Raghavan et al. (2010), and M-dwarfs (black dotted) from M. Janson et al. (2012). Each distribution is normalized to the observed binary fraction for that stellar type. Vertical solid lines mark estimated orbital separations for 5 of the 10 Group 2α CDG binaries with available astrometric parameters (see text for details). The hatched region spans the range of these systems (4900–41,000 au), illustrating that they lie in the very wide binary regime.

binary. This idea is supported by the work of C. Shariat et al. (2025), who used simulations including stellar evolution and orbital dynamics. Their results show that over half of solar-type triples undergo a merger of the inner binary within 12.5 Gyr, often due to eccentric Kozai–Lidov oscillations. The merged star remains in a wide binary with the third star.

The C. Shariat et al. (2025) models match many features of Group 2α CDGs, including wide orbital separations, merger timescales from hundreds of millions to several billion years, and merger products that lie on the giant branch. These postmerger stars are said to have distinct asteroseismic, photometric, and even astrometric signatures. Many of the white dwarf (WD)+MS merger products in their simulations are described as modified RG stars—with a dense core and an inflated envelope generated from the MS component—which may appear brighter than expected and show chemical signatures of internal processing. While detailed abundance predictions are not provided, the mixing of processed material from evolved components (e.g., WDs or RGB stars) naturally allows for enhanced N and Na, depleted C, and low ^{12}C/^{13}C ratios—consistent with the observed properties of CDGs. Simulated merger channels include both WD+RG and WD +MS systems, which are capable of producing core He-burning stars with elevated luminosities and evolved surface compositions. As mentioned in S. Maben et al. (2023a), detailed merger models using stellar evolution codes including nucleosynthesis can show chemical signatures similar to CDGs (e.g., X. Zhang & C. S. Jeffery 2013; X. Zhang et al. 2020).

As identified in S. Maben et al. (2023a), the mass distribution of Group 2 and 2α stars is a strong piece of evidence for these bright CDGs being merger products. They have an average mass around 1.6 $M_{\odot}$, with no stars below 1.0 $M_{\odot}$, and are more massive than typical RC stars (Table 3 and Figure 11). One natural interpretation for this bias toward higher masses is that the extra mass comes from combining two lower-mass stars through a merger.

Finally, the kinematics of Group 2α stars show that they are α enhanced yet have thin-disk orbital motions. This combination, while unusual, is seen in other studies (e.g., S. Nepal et al. 2024), and may be explained by radial migration. Our magnitude-limited sample also contributes, as nearby stars often reflect overlapping disk populations due to dynamical mixing.

In summary, the available evidence strongly favors a formation scenario in which Group 2 and 2α CDGs arise predominantly from binary mergers occurring within hierarchical triple systems. The relatively high overall binary fraction of about 60% supports this interpretation, since a pure binary merger population would be expected to have a near-zero binary fraction, as the binary would have merged, leaving only a single star. In the hierarchical triple scenario, the inner binary can merge, but the original tertiary companion remains, forming a wide binary system, as observed for at least 29% of our Group 2α sample. Alternative formation channels, such as AGB mass transfer or helium flash mixing, do not fully explain the observed chemical and orbital properties.

Given the incompleteness and observational biases in the current binary data, these conclusions remain tentative. Nonetheless, the hierarchical triple merger scenario currently provides the most consistent explanation for the properties of Group 2 and 2α CDGs. Future dedicated observations to better characterize binary fractions and orbital parameters will be essential to confirm or rule out this picture.

5. Conclusion

We have presented the first systematic asteroseismic analysis of the entire known population of CDGs, combining Kepler, K2, and TESS photometry for 129 stars. By measuring $\nu_{\rm max}$ and applying seismic scaling relations, we derived stellar masses and placed strong constraints on the evolutionary states of these chemically peculiar giants.

Our main findings are as follows:

1. We detect solar-like oscillations in 43 CDGs and, by measuring $\nu_{\rm max}$ and applying seismic scaling relations, determine precise masses for these stars. The majority ($\sim$79%) of these oscillating CDGs are low mass ($M \lesssim 2\,M_{\odot}$), in contrast to earlier suggestions that CDGs are predominantly intermediate-mass stars.
2. Our asteroseismic analysis reveals that most CDGs have $\nu_{\rm max}$ values lower than typical RC stars, and their luminosity distribution is distinctly bimodal. Together with their temperatures, these results indicate that the majority of CDGs are in the core He-burning or EAGB phases, with only a single clear RGB candidate in our sample.
3. Our expanded asteroseismic sample confirms the three chemically distinct groups of CDGs identified in S. Maben et al. (2023a), most clearly distinguished in the [Na/Fe] versus [C+N+O/Fe] abundance plane: Group 1 (normal [Na/Fe], scaled-solar [C+N+O/Fe]), Group 2 (enhanced [Na/Fe], scaled-solar [C+N+O/Fe]), and Group 2α (enhanced in both). We find that Group 2α is the α-enhanced analogs of Group 2, with enhanced initial C abundances explaining their extreme N enhancements.

4. Lithium enrichment is prevalent across all groups, linking CDGs to the broader population of lithium-rich giants and suggesting a common evolutionary channel.
5. We confirm that spectroscopic $\log g$ values are systematically offset from seismic values in CDGs, highlighting the necessity of asteroseismic constraints for accurate surface gravity and mass determination in these stars.
6. For single CDGs, expected and observed $\nu_{\rm max}$ values agree well. In contrast, binaries and multiple systems show systematic discrepancies, likely due to contamination affecting spectroscopic parameters. This underscores the importance of accounting for binarity in asteroseismic and spectroscopic analyses.
7. Significant observational biases—especially due to brightness and frequency resolution in TESS data—limit the detectability of $\nu_{\rm max}$ in our sample.
8. Our analysis supports distinct formation pathways for the different CDG groups, based on their updated classifications and orbital properties:
   1. *Group 1*. These are low-mass, Li-rich RC stars consistent with internal mixing during the core He-flash. Their moderate CN processing and solar [Na/Fe] abundances suggest in-situ processes without external mass transfer. Their normal mass and luminosity distributions suggest they are not merger products.
   2. *Groups 2 and 2*α. With a mass bias toward higher masses, these stars show strong chemical processing, with enhanced [Na/Fe] and strongly depleted [C/Fe]. Among the (identified) binaries in Group 2 α, a high fraction have very wide orbital separations. Together with the mass bias, this is consistent with formation through mergers in hierarchical triple systems, where the CDG originates from an inner binary merger, and the tertiary companion remains gravitationally bound.

This work provides the first large-scale asteroseismic mass constraints and a refined evolutionary framework for CDGs, resolving long-standing ambiguities about their nature and formation. In future work, we will use measurements of the large frequency separation ($\Delta\nu$) and period spacing of mixed modes (ΔP) to resolve remaining degeneracies in their evolutionary states and further constrain their internal structure. We are also constructing stellar merger models, which we will compare with the now substantial observational constraints. Continued time-domain photometry, high-resolution spectroscopy, and radial velocity monitoring will be important for fully characterizing the diversity and origins of this rare stellar population.

Acknowledgments

We sincerely thank the referee for valuable comments on the paper. This study is supported by the National Natural Science Foundation of China (NSFC) under grant No. 12588202 and National Key R&D Program of China Nos. 2023YFE0107800 and 2024YFA1611900. S.W.C. acknowledges federal funding from the Australian Research Council through a Future Fellowship (FT160100046) and Discovery Projects (DP190102431 and DP210101299). This research was partly supported by use of the Nectar Research Cloud, a collaborative Australian research platform supported by the National Collaborative Research Infrastructure Strategy (NCRIS). T.R.B. acknowledges support from the Australian Research Council through Laureate Fellowship FL220100117. S.M. thanks Raghubar Singh, Lupamudra Sarmah, and Zhuohan Li for helpful discussions. We thank Evgenii Neumerzhitckii for the use of his plotting routine.

This paper includes data collected by the Kepler mission and obtained from the MAST data archive at the Space Telescope Science Institute (STScI). Funding for the Kepler mission is provided by the NASA Science Mission Directorate. STScI is operated by the Association of Universities for Research in Astronomy, Inc., under NASA contract NAS 5–26555. This paper includes data collected with the TESS mission, obtained from the MAST data archive at the Space Telescope Science Institute (STScI). Funding for the TESS mission is provided by the NASA Explorer Program. STScI is operated by the Association of Universities for Research in Astronomy, Inc., under NASA contract NAS 5–26555.

This work has made use of data from the European Space Agency (ESA) mission Gaia (https://www.cosmos.esa.int/gaia), processed by the Gaia Data Processing and Analysis Consortium (DPAC, https://www.cosmos.esa.int/web/gaia/dpac/consortium). Funding for the DPAC has been provided by national institutions, in particular the institutions participating in the Gaia Multilateral Agreement.

Software:`Astropy` (Astropy Collaboration et al. 2013, 2018), `Lightkurve` (Lightkurve Collaboration et al. 2018), `Matplotlib` (J. D. Hunter 2007), `NumPy` (C. R. Harris et al. 2020), `Pandas` (W. McKinney 2010), `Python 3.12.2` (G. Van Rossum & F. L. Drake 2009), `SciPy` (P. Virtanen et al. 2020), `TOPCAT` (M. B. Taylor 2005).

Appendix A
Example Power Spectrum with Anomalous Peaks

Figure A1 shows the power spectrum of HD 124721, which exhibits anomalous peaks likely caused by contamination from a binary companion or hierarchical multiple system.

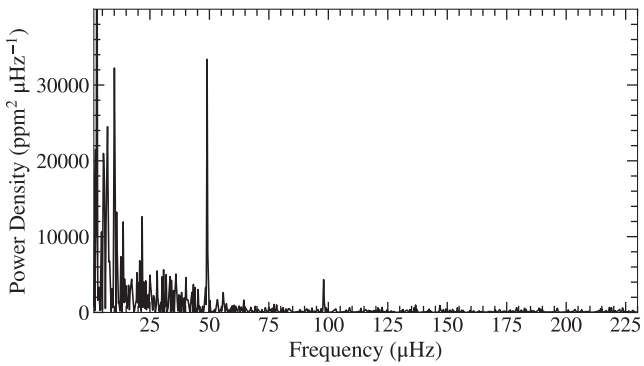

Figure A1. Power spectrum of HD 124721, a CDG with an anomalous peak at 50 μHz, calculated from a single sector of TESS data. The solar-like oscillations are centered at 35 μHz.

Appendix B
Asteroseismic Parameter Comparison

Table B1 lists literature asteroseismic parameters (ν_{max}, $\Delta\nu$, $\Delta\Pi_1$) alongside our pyMON-derived ν_{max} values for comparison, for our sample of 27 CDGs.

Table B1
Validation of Asteroseismic Parameters of the CDGs

CDGs Having Asteroseismic Parameters Derived from Kepler Light Curves in the Literature						
Star	KIC	K_p	$\nu_{max,\ lit}$ (a) (μHz)	$\Delta\nu_{lit}$ (μHz)	$\Delta\Pi_{1,lit}$ (s)	$\nu_{max,\ pyMON}$ (μHz)
2M19581582+4055411	5737930	9.95	3.49 ± 0.3 (b)	0.62 (b)	⋯	3.61 ± 0.17
2M19252454+4036484	5446927	11.76	21.88 ± 0.4	2.89 (c)	313 (c)	21.97 ± 0.10
2M19055092+3745351	2423824	11.05	22.02 ± 0.5	2.70 (c)	360 (c)	21.79 ± 0.12
2M19090355+4407005	8222189	9.84	23.02 ± 1.3	2.69 (a)	⋯	22.68 ± 0.36
2M19211488+3959431	4830861	11.11	25.94 ± 0.5	2.96 (a)	⋯	26.02 ± 0.14
2M19382715+3827580	3355015	11.90	26.98 ± 0.8	3.39 (c)	292 (c)	26.79 ± 0.13
2M19442885+4354544	8110538	12.85	28.77 ± 0.9	3.62 (d)	334 (d)	28.76 ± 0.15
2M19400612+3907470	4071012	10.94	29.20 ± 0.5	3.03 (d)	276 (d)	29.21 ± 0.14
2M19340082+4108491	5881715	11.46	30.90 ± 1.1	3.42 (c)	202 (c)	29.97 ± 0.24
2M19422093+5018436	11971123	11.08	32.47 ± 0.8	3.88 (d)	324 (d)	31.87 ± 0.24
2M19404764+3942376	4667911	10.50	36.37 ± 1.0	4.18 (d)	318 (d)	35.33 ± 0.24
2M19133911+4011046	5000307	11.23	42.16 ± 0.6	4.74 (c)	324 (c)	41.85 ± 0.18
2M19181645+4506527	8879518	10.98	46.18 ± 0.8	4.65 (d)	268 (d)	45.21 ± 0.22
2M19125144+3850261	3736289	10.85	49.94 ± 1.3	4.99 (c)	307 (c)	49.09 ± 0.24
2M19565550+4330561	7848354	13.12	51.74 ± 1.5	4.67 (a)	⋯	50.74 ± 0.29
2M19052312+4422242	8352953	11.68	230.27 ± 2.9	16.73 (a)	⋯	230.13 ± 0.40
CDGs having asteroseismic parameters derived from TESS light curves in the literature						
Star	TIC	Tmag	$\nu_{max,\ lit}$ (μHz)	$\Delta\nu_{lit}$ (μHz)	$N_{sectors}$	$\nu_{max,\ pyMON}$ (μHz)
BD+5 593	283623989	8.03	23.50 ± 3.7 (e)	⋯	2	20.95 ± 0.51
HD 56438	134545196	7.06	23.80 ± 3.7 (e)	⋯	7	23.03 ± 0.86
HD 18474	192247771	4.63	25.14 ± 1.7 (f)	2.70 ± 0.4 (f)	2	25.29 ± 0.48
2M05120630-5913438	358459098	9.91	25.40 ± 3.0 (e)	⋯	9	18.95 ± 0.42
2M06022767-6209038	149989441	10.01	29.50 ± 4.5 (e)	⋯	8	23.00 ± 0.77
HD 124721	242443733	8.60	29.90 ± 2.9 (e)	⋯	2	34.72 ± 1.03
HD 201557	231638013	8.29	31.50 ± 1.4 (f)	2.99 ± 0.2 (f)	2	31.74 ± 0.30
HD 16424	441127020	8.62	31.60 ± 2.3 (e)	⋯	2	37.27 ± 0.34
HD 18636	321087542	6.80	36.60 ± 2.4 (e)	⋯	4	32.52 ± 0.69
HD 40402	153122373	7.75	38.10 ± 4.5 (e)	⋯	2	44.56 ± 0.34
HD 166208	332626441	4.19	48.73 ± 2.7 (f)	4.35 ± 0.5 (f)	7	48.03 ± 1.26

Note. All stellar designations beginning with "2M" denote the APOGEE ID of carbon-deficient giants. Kepler Input Catalog (KIC). TESS Input Catalog (TIC).
Reference. (a) J. Yu et al. (2018), (b) J. Yu et al. (2020), (c) B. Mosser et al. (2014), (d) M. Vrard et al. (2016), (e) M. Hon et al. (2021), (f) J. Zhou et al. (2024).

(This table is available in machine-readable form in the online article.)

Appendix C
Marginal Detections and Nondetections

Tables C1 and C2 present atmospheric parameters for CDGs with marginal detections and nondetections of solar-type oscillations, respectively.

Table C1
Atmospheric Parameters of the CDGs with Marginal Detections

Star	TIC	*T*mag	$T_{\rm eff}$ (K)	log *g*	$\log(L/L_{\odot})$
HD 120213	418654329	4.55	4577	1.95	2.80
HD 119256	453698438	6.23	4984	2.64	2.89
HD 67728	299844351	6.53	4827	2.28	2.82
HD 215974	44088493	7.58	…	…	2.15
HD 132776	157884863	7.77	4680	2.30	2.10
2M19104331+2657415	407250258	10.44	5007	2.56	2.08
2M05262269+2913054	285638910	11.55	4603	1.85	2.10
2M06282805-3106253	29629380	12.11	5037	2.25	2.24
2M01001653+6017239	256105839	12.40	4542	1.94	2.41

Note. All stellar designations beginning with "2M" denote the APOGEE ID of carbon-deficient giants. TESS Input Catalog (TIC).

(This table is available in machine-readable form in the online article.)

Table C2
Atmospheric Parameters of the CDGs with No Detectable Oscillations

Star	KIC/EPIC/TIC	$K_{\rm p}$/*T*mag	$T_{\rm eff}$ (K)	log *g*	$\log(L/L_{\odot})$
2M19522952+4210399[a]	6717417	12.10	5111	2.86	1.69
HD 120170	212678022	8.87	5127	2.76	2.07
37 Com	165945199	3.82	4610	2.50	2.66
HD 26575	168751697	5.50	4690	2.20	2.39
HD 21018	302769337	5.63	5310	1.60	2.39
HD 31274	161476030	6.24	…	…	2.34
HD 20090	441510543	6.96	…	…	2.44
HD 28932	452783241	7.00	4915	2.50	2.30
HD 17232	36819972	7.14	…	…	3.07
HD 36552	354518979	7.28	…	…	2.06
CD-2875	246820962	7.43	…	…	3.35
HD 30297	286451983	7.53	…	…	2.00
HD 198718	91434822	7.76	4980	2.50	2.10
HD 204046	211407433	7.90	4984	2.51	2.27
HD 105783	22026413	8.00	4860	2.10	2.20
HD 207774	883711	8.06	5125	2.79	2.09
CD-377613	165534155	8.95	…	…	2.04
2M04495090+3851461	187205131	9.36	4863	2.34	2.22
BD -19 967	121564557	9.36	…	…	1.82
2M07581022+4325398	141071795	9.40	4969	2.42	2.04
2M02491557+5147498	428071324	9.57	4687	2.04	2.67
2M08445468+2957159	117280852	9.71	5052	3.07	1.39
2M06362656-6347360	293347406	10.00	5221	2.42	2.17
2M03370386+6830247	275911107	10.27	5220	2.48	1.91
2M23540193+5649215	444325050	10.53	4245	1.22	3.01
2M16055395+2356168	236323154	10.83	4969	2.42	2.25
2M23065670+4724235	173298845	11.00	4795	2.07	2.26
2M05524283+2648348	77824724	11.20	3955	0.76	2.68
2M05323558+3213532	115055396	11.33	4451	1.44	2.34
2M05294163+3942524	368147062	11.41	4989	2.22	2.32

Table C2
(Continued)

Star	KIC/EPIC/TIC	K_p/*T*mag	T_{eff} (K)	log *g*	log($L/L_\odot$)
2M05501847-0010369	176615527	11.47	4070	0.94	2.89
2M20564714+5013372	313233284	11.53	4059	1.11	2.51
2M07514685-6416532	410446741	11.54	4986	3.06	1.40
2M04482937+6336236	66216687	11.55	4995	2.51	1.82
2M06572928-2942235	62965851	11.56	4860	2.10	2.08
2M07084597-6227180	349056525	11.62	4987	2.22	2.15
2M05491338-6528536	149627133	11.74	4795	2.47	1.74
2M04572716+2503506	60604623	11.82	5012	2.24	2.03
2M00290504+4952279	202643399	11.93	4841	2.35	1.82
2M07442293-2344132	140539531	11.94	5074	2.65	2.00
2M23552546+7455247	426145258	12.05	4965	2.46	1.78
2M03345798+6800254	85508309	12.12	4577	1.66	2.52
2M00254993+7357163	407461210	12.13	5045	2.53	2.17
2M00220008+6915238	407116170	12.17	4098	1.08	2.57
2M04303772+6042173	65781276	12.29	4886	2.46	1.80
2M06383118+4646336	190378881	12.34	4858	2.16	2.04
2M01450782+6445416	399264249	12.38	4392	1.63	2.29
2M21184119+4836167	63158860	12.48	4199	1.25	1.63
2M02073982+3707297	184653921	12.52	4993	2.16	2.31
2M04592354-5907517	220460842	12.58	4960	2.96	1.42
2M05481354+2926231	76540894	12.64	4720	2.12	2.19
2M03394392+6932532	276033754	12.68	5005	2.37	1.91
2M04403830+2554274	150095560	12.75	4992	2.41	1.78
2M05261122+2914086	285471851	12.76	4913	2.13	2.08
2M02461527+6024099	50766398	12.81	5092	2.52	1.87
2M06475248+1837026	57130767	12.86	4803	1.85	2.61
2M07061526-1526100	148579421	12.97	4601	1.94	2.26
2M19181713+2703269	404209613	12.97	4641	2.17	2.25
2M12261419-6325497	450565123	12.98	4667	2.01	4.66
2M21405264+6021011	406519141	13.01	5033	2.44	2.26
2M12254845-6228451	450475155	13.06	4820	2.43	2.73
2M23461558-1711228	2762370	13.14	4308	1.16	2.57
2M03431471+6657575	276191898	13.18	5124	2.44	1.91
2M05155141+4608365	368180782	13.26	4987	2.52	2.42
2M04154135-7223426	33835137	13.38	5337	2.65	1.84
2M06242370+0556213	234571169	13.49	5007	2.61	2.14
2M10005815-5533520	462058180	13.69	4986	2.12	3.60
2M07171291-3935510	22974233	13.81	4949	2.09	2.00
2M06144688+1544582	434369521	13.87	4706	2.12	1.88
2M08234846-4918149	388755202	14.10	5012	2.14	2.33
2M10552602-5856257	459848103	14.12	4980	2.32	3.52
2M23041065-2410260	12970956	14.24	4480	1.43	1.79
2M10042811-5526077	462394241	14.35	4939	2.47	3.48
2M06295110+1158423	207012381	14.68	4981	2.43	1.62
2M06414471+0138421	301589301	14.82	5055	2.94	1.66
2M10041347-5515019	462361790	15.26	4942	2.55	2.76
2M09102427-4824543	355666181	15.44	4457	1.56	2.64

Note. All stellar designations beginning with "2M" denote the APOGEE ID of carbon-deficient giants. The first row contains Kepler Input Catalog (KIC) ID, the second row contains the K2 Ecliptic Plane Input Catalog (EPIC) ID, while the remaining rows contain TESS Input Catalog (TIC) IDs. Horizontal lines are used to visually separate stars observed with Kepler and K2 from those observed with TESS.
[a] Pulsating star.

(This table is available in machine-readable form in the online article.)

Appendix D
Examples of Oscillation Power Spectra

Figure D1 shows example power spectra for eight CDGs observed with Kepler and TESS. These stars span a range of $\nu_{\rm max}$ values.

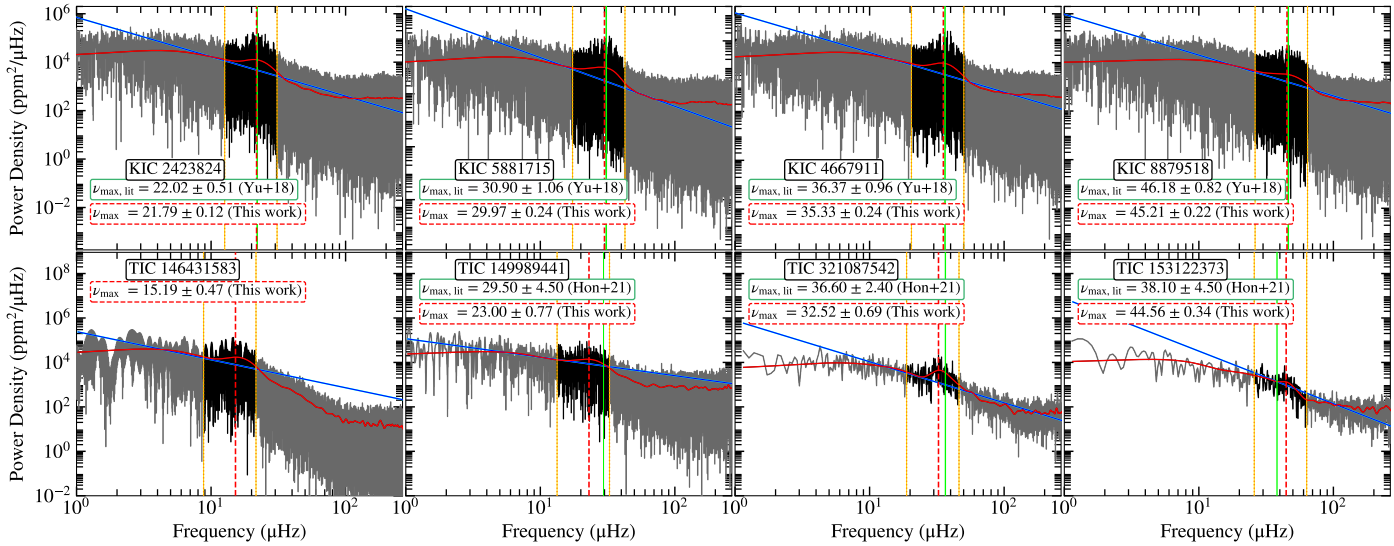

Figure D1. Power spectra of eight CDGs (gray) using Kepler (top panel) and TESS data (bottom panel). The smoothed power spectrum is shown in red, and the linear background fit in blue. The power excess window is shaded black and bounded by vertical yellow lines. Vertical red dashed lines indicate the measured $\nu_{\rm max}$ values using the `pyMON` pipeline. For stars with literature $\nu_{\rm max}$ values (e.g., J. Yu et al. 2018; M. Hon et al. 2021), these are shown as vertical green lines.

ORCID iDs

Sunayana Maben https://orcid.org/0000-0001-9974-1754
Timothy R. Bedding https://orcid.org/0000-0001-5222-4661
Gang Zhao https://orcid.org/0000-0002-8980-945X
Madeline Howell https://orcid.org/0000-0003-0929-6541
Bacham E. Reddy https://orcid.org/0000-0001-9246-9743

References

Abdurro'uf, Accetta, K., Aerts, C., et al. 2022, ApJS, 259, 35
Adamczak, J., & Lambert, D. L. 2013, ApJ, 765, 155
Adibekyan, V. Z., Santos, N. C., Sousa, S. G., & Israelian, G. 2011, A&A, 535, L11
Alonso, A., Arribas, S., & Martínez-Roger, C. 1999, A&AS, 140, 261
Ash, A. L., Pinsonneault, M. H., Vrard, M., & Zinn, J. C. 2025, ApJ, 979, 135
Astropy Collaboration, Robitaille, T. P., Tollerud, E. J., et al. 2013, A&A, 558, A33
Astropy Collaboration, Price-Whelan, A. M., Sipőcz, B. M., et al. 2018, AJ, 156, 123
Bailer-Jones, C. A. L., Rybizki, J., Fouesneau, M., Demleitner, M., & Andrae, R. 2021, AJ, 161, 147
Bidelman, W. P. 1951, ApJ, 113, 304
Bidelman, W. P., & MacConnell, D. J. 1973, AJ, 78, 687
Bond, H. E. 2019, ApJ, 887, 12
Brown, J. A., Sneden, C., Lambert, D. L., & Dutchover, E., Jr. 1989, ApJS, 71, 293
Brown, T. M., Gilliland, R. L., Noyes, R. W., & Ramsey, L. W. 1991, ApJ, 368, 599
Caldwell, D. A., Tenenbaum, P., Twicken, J. D., et al. 2020, RNAAS, 4, 201
Cannon, A. J., & Pickering, E. C. 1912, AnHar, 56, 65-114
Casey, A. R., Ho, A. Y. Q., Ness, M., et al. 2019, ApJ, 880, 125
Caughlan, G. R. 1965, ApJ, 141, 688
Chaplin, W. J., & Miglio, A. 2013, ARA&A, 51, 353
Chontos, A., Huber, D., Sayeed, M., & Yamsiri, P. 2022, JOSS, 7, 3331
Colman, I. L., Huber, D., Bedding, T. R., et al. 2017, MNRAS, 469, 3802
De Rosa, R. J., Patience, J., Wilson, P. A., et al. 2014, MNRAS, 437, 1216
Deupree, R. G., & Wallace, R. K. 1987, ApJ, 317, 724
Dommanget, J., & Nys, O. 2002, yCat, I/274
Dupuy, T. J., & Liu, M. C. 2011, ApJ, 733, 122
El-Badry, K., Rix, H.-W., & Heintz, T. M. 2021, MNRAS, 506, 2269
Gaia Collaboration 2022, yCat, 1358,0
Gaia Collaboration, Brown, A. G. A., Vallenari, A., et al. 2018, A&A, 616, A1
Gaia Collaboration, Prusti, T., de Bruijne, J. H. J., et al. 2016, A&A, 595, A1
Gaia Collaboration, Vallenari, A., Brown, A. G. A., et al. 2023, A&A, 674, A1
Girardi, L. 2016, ARA&A, 54, 95
Green, G. M., Schlafly, E., Zucker, C., Speagle, J. S., & Finkbeiner, D. 2019, ApJ, 887, 93
Grevesse, N., Asplund, M., & Sauval, A. J. 2007, SSRv, 130, 105
Harris, C. R., Millman, K. J., van der Walt, S. J., et al. 2020, Natur, 585, 357
Hekker, S., & Johnson, J. A. 2019, MNRAS, 487, 4343
Holanda, N., Drake, N. A., & Pereira, C. B. 2023, MNRAS, 518, 4038
Holanda, N., Flaulhabe, T., Quispe-Huaynasi, F., Sonally, A., & Pereira, C. B. 2024, ApJ, 971, 152
Holberg, J. B., Oswalt, T. D., Sion, E. M., Barstow, M. A., & Burleigh, M. R. 2013, MNRAS, 435, 2077
Holtzman, J. A., Hasselquist, S., Shetrone, M., et al. 2018, AJ, 156, 125
Hon, M., Huber, D., Kuszlewicz, J. S., et al. 2021, ApJ, 919, 131
Howell, M., Campbell, S. W., Kalup, C., Stello, D., & De Silva, G. M. 2025, MNRAS, 536, 1389
Howell, M., Campbell, S. W., Stello, D., & De Silva, G. M. 2022, MNRAS, 515, 3184
Howell, M., Campbell, S. W., Stello, D., & De Silva, G. M. 2024, MNRAS, 527, 7974
Huang, C. X., Vanderburg, A., Pál, A., et al. 2020a, RNAAS, 4, 204
Huang, C. X., Vanderburg, A., Pál, A., et al. 2020b, RNAAS, 4, 206
Huber, D., Bedding, T. R., Stello, D., et al. 2011, ApJ, 743, 143
Huber, D., Stello, D., Bedding, T. R., et al. 2009, CoAst, 160, 74
Hunter, J. D. 2007, CSE, 9, 90
Iben, I., & Renzini, A. 1984, PhR, 105, 329
Iben, I., Jr. 1967, ApJ, 147, 624
Izzard, R. G., Jeffery, C. S., & Lattanzio, J. 2007, A&A, 470, 661
Janson, M., Hormuth, F., Bergfors, C., et al. 2012, ApJ, 754, 44
Jenkins, J. M., Caldwell, D. A., Chandrasekaran, H., et al. 2010, ApJL, 713, L87
Jenkins, J. M., Twicken, J. D., McCauliff, S., et al. 2016, Proc. SPIE, 9913, 99133E

Jofré, P., Jorissen, A., Van Eck, S., et al. 2016, A&A, 595, A60
Karakas, A. I., & Lattanzio, J. C. 2014, PASA, 31, e030
Kervella, P., Arenou, F., Mignard, F., & Thévenin, F. 2019, A&A, 623, A72
Kervella, P., Arenou, F., & Thévenin, F. 2022, A&A, 657, A7
Kjeldsen, H., & Bedding, T. R. 1995, A&A, 293, 87
Kovaleva, D., Kaygorodov, P., Malkov, O., Debray, B., & Oblak, E. 2015, A&C, 11, 119
Kumar, Y. B., Reddy, B. E., Campbell, S. W., et al. 2020, NatAs, 4, 1059
Kumar, Y. B., Reddy, B. E., & Lambert, D. L. 2011, ApJL, 730, L12
Li, Y., Bedding, T. R., Murphy, S. J., et al. 2022, NatAs, 6, 673
Lightkurve Collaboration, Cardoso, J. V. d. M., Hedges, C., et al., 2018 Lightkurve: Kepler and TESS Time Series Analysis in Python, Astrophysics Source Code Library, ascl:1812.013
Luck, R. E., & Heiter, U. 2007, AJ, 133, 2464
Luger, R., Agol, E., Kruse, E., et al. 2016, AJ, 152, 100
Maben, S., Campbell, S. W., Kumar, Y. B., Reddy, B. E., & Zhao, G. 2023a, ApJ, 957, 18
Maben, S., Kumar, Y. B., Reddy, B. E., Campbell, S. W., & Zhao, G. 2023b, MNRAS, 525, 4554
Malla, S. P., Stello, D., Montet, B. T., et al. 2024, MNRAS, 534, 1775
Martell, S. L., & Shetrone, M. D. 2013, MNRAS, 430, 611
Mason, B. D., Wycoff, G. L., Hartkopf, W. I., Douglass, G. G., & Worley, C. E. 2001, AJ, 122, 3466
Masseron, T., & Hawkins, K. 2017, A&A, 597, L3
Matsuno, T., Starkenburg, E., Balbinot, E., & Helmi, A. 2024, A&A, 685, A59
McKinney, W. 2010, in 9th Python in Science Conf., ed. S. van der Walt & J. Millman (Austin, TX: SciPy), 56
Mocák, M., Müller, E., Weiss, A., & Kifonidis, K. 2009, A&A, 501, 659
Morel, T., Miglio, A., Lagarde, N., et al. 2014, A&A, 564, A119
Mori, K., Kusakabe, M., Balantekin, A. B., Kajino, T., & Famiano, M. A. 2021, MNRAS, 503, 2746
Mosser, B., Benomar, O., Belkacem, K., et al. 2014, A&A, 572, L5
Nepal, S., Chiappini, C., Queiroz, A. B., et al. 2024, A&A, 688, A167
Nissen, P. E. 2004, in Origin and Evolution of the Elements, ed. A. McWilliam & M. Rauch (Cambridge: Cambridge Univ. Press), 154
Palacios, A., Jasniewicz, G., Masseron, T., et al. 2016, A&A, 587, A42
Palacios, A., Parthasarathy, M., Bharat Kumar, Y., & Jasniewicz, G. 2012, A&A, 538, A68
Parker, R. J., & Meyer, M. R. 2014, MNRAS, 442, 3722
Pinsonneault, M. H., Elsworth, Y., Epstein, C., et al. 2014, ApJS, 215, 19
Pinsonneault, M. H., Elsworth, Y. P., Tayar, J., et al. 2018, ApJS, 239, 32
Prša, A., Harmanec, P., Torres, G., et al. 2016, AJ, 152, 41
Raghavan, D., McAlister, H. A., Henry, T. J., et al. 2010, ApJS, 190, 1
Riello, M., De Angeli, F., Evans, D. W., et al. 2021, A&A, 649, A3
Rui, N. Z., & Fuller, J. 2021, MNRAS, 508, 1618
Schlafly, E. F., & Finkbeiner, D. P. 2011, ApJ, 737, 103
Schlegel, D. J., Finkbeiner, D. P., & Davis, M. 1998, ApJ, 500, 525
Schwab, J. 2020, ApJL, 901, L18
Serenelli, A., Johnson, J., Huber, D., et al. 2017, ApJS, 233, 23
Shariat, C., Naoz, S., El-Badry, K., et al. 2025, ApJ, 978, 47
Smith, J. C., Stumpe, M. C., Van Cleve, J. E., et al. 2012, PASP, 124, 1000
Sparke, L. S., & Gallagher, J. S. I. 2007, Galaxies in the Universe,
Stello, D., Bruntt, H., Preston, H., & Buzasi, D. 2008, ApJL, 674, L53
Stello, D., Chaplin, W. J., Basu, S., Elsworth, Y., & Bedding, T. R. 2009, MNRAS, 400, L80
Stello, D., Saunders, N., Grunblatt, S., et al. 2022, MNRAS, 512, 1677
Stetson, P. B. 2000, PASP, 112, 925
Taylor, M. B. 2005, in ASP Conf. Ser. 347, Astronomical Data Analysis Software and Systems XIV, ed. P. Shopbell, M. Britton, & R. Ebert (San Francisco, CA: ASP), 29
Vanderburg, A., & Johnson, J. A. 2014, PASP, 126, 948
Van Rossum, G., & Drake, F. L. 2009, Python 3 Reference Manual (Scotts Valley, CA: CreateSpace)
Venn, K. A., Irwin, M., Shetrone, M. D., et al. 2004, AJ, 128, 1177
Virtanen, P., Gommers, R., Oliphant, T. E., et al. 2020, NatMe, 17, 261
Vrard, M., Mosser, B., & Samadi, R. 2016, A&A, 588, A87
Yan, H.-L., Zhou, Y.-T., Zhang, X., et al. 2021, NatAs, 5, 86
Yu, J., Bedding, T. R., Stello, D., et al. 2020, MNRAS, 493, 1388
Yu, J., Huber, D., Bedding, T. R., et al. 2018, ApJS, 236, 42
Zhang, X., & Jeffery, C. S. 2013, MNRAS, 430, 2113
Zhang, X., Jeffery, C. S., Li, Y., & Bi, S. 2020, ApJ, 889, 33
Zhou, J., Bi, S., Yu, J., et al. 2024, ApJS, 271, 17